NEUROSCIENCE

Mice lacking acid-sensing ion channel 2 in the medial prefrontal cortex exhibit social dominance

Boren Lin[1,2], Zhen Jin[1], Gyeongah Park[1], Qian Ge[1], Kritika Singh[2], William G. Ryan V[3], Ali Sajid Imami[3], Farzaneh Naghavi[3], Olivia Ann Miller[2], Saira Khan[2], Hui Lu[4], Robert E. McCullumsmith[3,5], Jianyang Du[1,6]*

Social dominance is essential for maintaining a stable society and has both positive and negative impacts on social animals, including humans. However, the regulatory mechanisms governing social dominance, as well as the crucial regulators and biomarkers involved, remain poorly understood. We discover that mice lacking acid-sensing ion channel 2 (ASIC2) exhibit persistently higher social dominance than their wild-type cagemates. Conversely, overexpression of ASIC2 in the medial prefrontal cortex reverses the dominance hierarchy observed in ASIC2 knockout (*Asic2*$^{-/-}$) mice. *Asic2*$^{-/-}$ neurons exhibit increased synaptic transmission and plasticity, potentially mediated by protein kinase A signaling pathway. Furthermore, ASIC2 plays distinct functional roles in excitatory and inhibitory neurons, thereby modulating the balance of neuronal activities underlying social dominance behaviors—a phenomenon suggestive of a cell subtype–specific mechanism. This research lays the groundwork for understanding the mechanisms of social dominance, offering potential insights for managing social disorders, such as depression and anxiety.

INTRODUCTION

Social ranking is substantial for humans due to evolutionary advantages linked to resource access and survival, providing structure and order in societies, offering a sense of identity and belonging, and serving as motivation. While it can bring clarity and predictability to social interactions and is reinforced by cultural, economic, and political factors, excessive emphasis on it can lead to negative outcomes like inequality and stress. Social status–based dominance is linked to various physiological and psychological diseases. In human society, those with low social ranking often show a heightened vulnerability to illnesses. For example, studies have highlighted social ranking as a predictor of susceptibility to chronic stress (*1*). People with higher socioeconomic status tend to live longer, enjoy better well-being and have reduced incidences of stress-related diseases such as cardiovascular diseases and type 2 diabetes (*2*). In addition, individuals in dominant positions show a lower risk of psychiatric disorders compared to those in subordinate roles (*3*, *4*). Yet, despite its significance, our understanding of the mechanisms underlying social dominance remains limited.

Group-housed mice are widely recognized to naturally establish hierarchies, making them a valuable laboratory model for studying the mechanism of social dominance (*5*, *6*). Recent studies have introduced established reliable behavioral assays, such as the tube test, warm spot, etc., to evaluate mouse social dominance behaviors (*7*–*11*). Studies focusing on the prelimbic (PL) area of the medial prefrontal cortex (mPFC) in stable dominance have shown enhanced synaptic strength in dominant mice compared to the subordinates using electrophysiology assays (*7*–*11*). Manipulating α-amino-3-hydroxy-5-methyl-4-isoxazolepropionic acid (AMPA) receptor (AMPAR)–mediated synaptic transmission using virus-based tools was sufficient to influence social rankings in the dominance test (*7*–*9*). While these pioneering studies have provided crucial insight into the formation of social dominance in mice, many questions persist, such as identifying the synaptic molecules and signaling pathways that determine social rankings, recognizing the relevant mPFC circuits affecting social ranking, and pinpointing potential biomarkers that regulate social dominance and could serve as the therapeutic targets.

We recently discovered that proton (H^+) receptors, specifically ASICs, play a vital role in reinforcing social dominance in mice. This suggests that ASIC-dependent signaling pathways are involved in shaping and manifesting social dominance. Previous studies demonstrated that H^+ is a potential neurotransmitter that activates postsynaptic ASICs to regulate synaptic transmission and plasticity (*12*–*14*). While the extracellular pH in the brain is typically maintained within a small range through homeostatic processes, neuronal activity can cause transient and localized pH fluctuations (*15*). ASICs are members of the Degenerin/Epithelial Na^+ channel (DEG/ENaC) family, with six identified genes (*Asic 1a, 1b, 2a, 2b, 3*, and *4*) (*16*, *17*). In the brain, ASIC1a and ASIC2 are the two major subunits that assemble as homo- or heterotrimers to form acid-activated cation channels (*18*–*21*). Studies in various brain areas indicate that presynaptic stimulation induces ASIC-like excitable postsynaptic currents (EPSCs) in pyramidal neurons. Impaired ASIC function leads to decreased long-term potentiation (LTP) (*12*, *22*). Moreover, ASICs influence a spectrum of emotional behaviors in mice, from chronic stress response (*23*, *24*) and social interaction (*25*) to aggression (*26*), fear learning and memory (*27*–*30*), cocaine-seeking (*31*), and even anxiety and depression (*32*). The impacts of ASIC1a and ASIC2 differ due to their different pH sensitivity and varied expression across brain regions (*33*). Collectively, this evidence proposes a pivotal role for ASICs in orchestrating neuronal activities linked to behaviors underpinning social dominance.

[1]Department of Anatomy and Neurobiology, University of Tennessee Health Science Center, Memphis, TN 38163, USA. [2]Department of Biological Sciences, University of Toledo, Toledo, OH 43606, USA. [3]Department of Neuroscience, University of Toledo, Toledo, OH 43606, USA. [4]Department of Pharmacology and Physiology, George Washington University School of Medicine, Washington, DC 20037, USA. [5]Neurosciences Institute, ProMedica, Toledo, OH 43614, USA. [6]Neuroscience Institute, University of Tennessee Health Science Center, Memphis, TN 38163, USA.
*Corresponding author. Email: jdu15@uthsc.edu

Here, our findings reveal that *Asic2*$^{-/-}$ mice display decreased hierarchical stability within their groups and attained a higher social ranking compared to their wild-type (WT) cagemates, suggesting an ASIC2-dependent mechanism in social dominance. In addition, the role of ASICs in regulating social dominance is linked to their control of glutamate receptor (GluR)–dependent synaptic transmission and plasticity in the mPFC. We have also identified a protein kinase A (PKA)-dependent signaling pathway in which ASIC2 regulates synaptic activity associated with social dominance. When ASIC2 is solely deleted from excitatory or inhibitory neurons in the mPFC, it distinctly influences social dominance, underscoring the specific role of ASIC2 in governing neuronal functions related to social dominance.

RESULTS

Deletion of ASIC2 in mice raises the social ranking

The tube test assay assesses the relative social ranking between two mice by placing them on opposite ends of an open tube to create a nonviolent conflict situation in which the dominant animal tends to force the subordinate opponent to retreat (*7*–*9*, *11*, *34*) (Fig. 1A). A group of four age- and sex-matched mice were housed together for 2 weeks and subjected to the tube test. Most of the mice groups can form stable-ranking organizations with three subtypes, linear types were most common, while despotic and single-slave types were rarer. Very few mice exhibited nonstable ranking (fig. S1A). While both male and female mice can establish a stable social dominance, females were less likely to form a linear ranking (fig. S1B) (*6*). To streamline our analysis of social dominance, we predominantly focused on male mice known for their stable linear social ranking. A group of four *Asic2*$^{-/-}$ mice ($n = 28$ cages) exhibited a lower success rate in establishing stable social ranking compared to the WT counterparts ($n = 45$ cages), which implies that the deletion of ASIC2 in mice may interrupt the social dominance patterns (fig. S1C).

Asic2$^{-/-}$ mice demonstrated no difference in locomotion or movement compared to WT mice in the open-field test (fig. S2, A and B, $n = 13$ mice in each group). In addition, *Asic2*$^{-/-}$ mice exhibit no significant changes in center time compared to WT mice, indicating no observable changes in anxiety-like behaviors among the *Asic2*$^{-/-}$ mice (fig. S2C). We housed one *Asic2*$^{-/-}$ male mouse together with three male WTs for 2 weeks followed by a round-robin tube test tournament, wherein every mouse in the cage competes against each of the other three mice once daily (one trial) for a total of 7 days (trials) ($n = 7$ cages). *Asic2*$^{-/-}$ mice won the tube

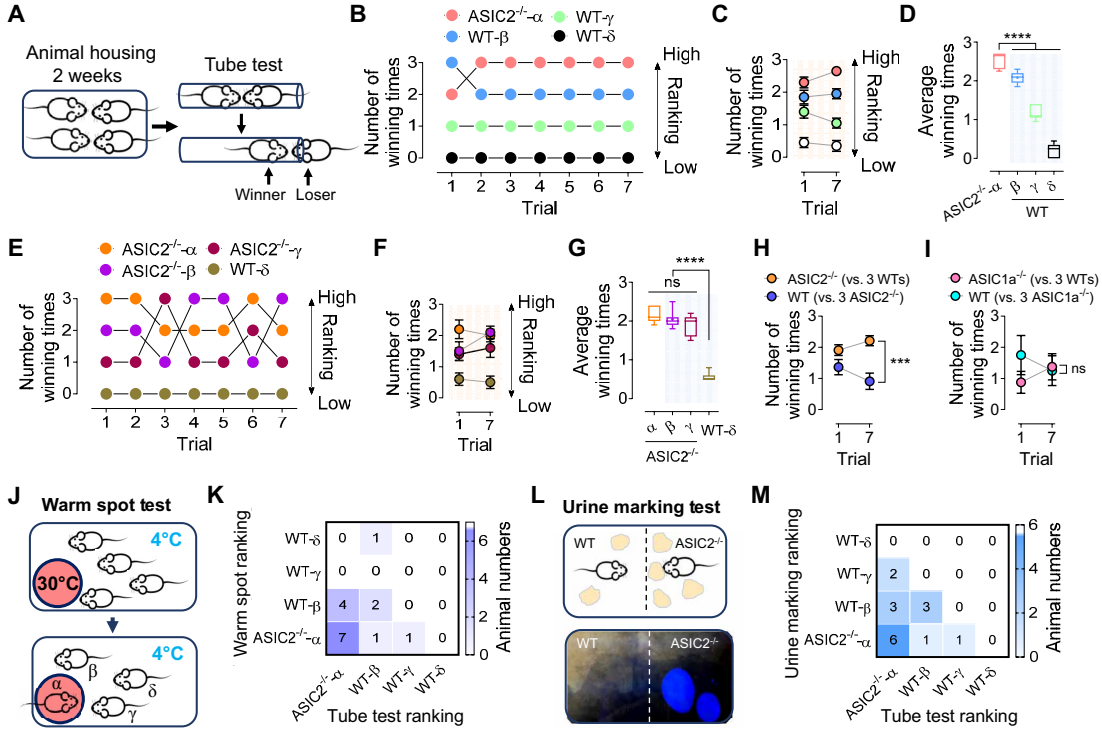

Fig. 1. *Asic2*$^{-/-}$ mice exhibit a superior social ranking compared to their WT cagemates in dominance behavior tests. (**A**) Protocol of mouse tube test assay. Four mice housed together for 2 weeks undergo a round-robin tournament to determine social ranking. (**B**) Typical ranking of a group of one *Asic2*$^{-/-}$ mouse versus three WT cagemates. (**C**) Average number of winning times in trials 1 and 7. (**D**) Comparison of winning times between WT and *Asic2*$^{-/-}$ mice shows that *Asic2*$^{-/-}$ mice have higher winning times. ****$P < 0.0001$, one-way ANOVA. $n = 28$ cages. (**E**) Typical ranking of three *Asic2*$^{-/-}$ mice versus one WT cagemate. (**F**) Average number of winning times in trials 1 and 7. (**G**) Three *Asic2*$^{-/-}$ mice exhibit higher winning times than one WT cagemate. ****$P < 0.0001$; ns, nonsignificant, one-way ANOVA. $n = 7$ cages. (**H**) Comparison of winning times between groups of one *Asic2*$^{-/-}$ mouse versus three WT cagemates and one WT mouse versus three *Asic2*$^{-/-}$ cagemates, using data from (B) to (G). ***$P = 0.0007$, two-tailed unpaired Student's *t* test. (**I**) Comparison of winning times between groups of one *Asic1a*$^{-/-}$ mouse versus three WT cagemates, and one WT mouse versus three *Asic1a*$^{-/-}$ cagemates. ns, $P = 0.8477$, two-tailed unpaired Student's *t* test. $n = 7$ cages. (**J** and **K**) Schematic of mouse warm spot test and correlation with tube test rank. $P = 0.0118$, two-sided Fisher's exact test. $n = 16$ cages. (**L** and **M**) Schematic of mouse urine marking test and correlation with tube test rank. $P = 0.0118$, two-sided Fisher's exact test. $n = 16$ cages.

test over at least two WT mice (Fig. 1, B to D). A parallel experiment in cages housing three *Asic2*$^{-/-}$ mice and one WT mouse ($n = 7$ cages) further confirmed that *Asic2*$^{-/-}$ mice consistently scored higher victory counts than the WT mice (Fig. 1, E to G). This observation was echoed by the average number of winner times on two group configurations—one *Asic2*$^{-/-}$ mouse versus three WT mice group (Fig. 1, B to D), and three *Asic2*$^{-/-}$ mice versus one WT mouse (Fig. 1, E to G), as summarized in Fig. 1H. In contrast, *Asic1a*$^{-/-}$ mice did not exhibit a similar trend (Fig. 1I)—one *Asic1a*$^{-/-}$ mouse versus three WT mice group, and three *Asic1a*$^{-/-}$ mice versus one WT mouse group ($n = 7$ cages).

Such hierarchical order was confirmed by a warm spot test (Fig. 1J) (*8*), conducted in the group consisting of one *Asic2*$^{-/-}$ mouse versus three WT mice ($n = 16$ cages). Mice identified as ranked α and β by the tube test and warm spot tests were classified as high and ranked γ and δ as low, and Fisher's exact test suggests a significant difference in the contingency between these two assays ($P = 0.0118$), demonstrating a high social dominance in *Asic2*$^{-/-}$ mice, concurring with the observation from the tube tests (Fig. 1K). Consistently, results obtained from territory urine marking tests ($n = 16$ cages) suggest a similar hierarchical relationship in the groups assessed by tube tests ($P = 0.0188$) (Fig. 1, L and M).

To detect whether the increase of dominance in the *Asic2*$^{-/-}$ mice is the result of elevated aggression, adult males from a pool of WT or *Asic2*$^{-/-}$ mice were also subjected to the resident-intruder test, a standardized method to measure offensive aggression and defensive behavior (fig. S3A, $n = 16$ cages). According to the analysis of latency, the number of attacks, and the number of vocals, increased dominance in *Asic2*$^{-/-}$ mice did not correlate with increased aggressiveness (fig. S3, B to D). These data are expected, as high levels of aggression are not always associated with a stable high dominance in rodents (*35*). We subsequently examined whether knocking out ASIC2 increases mice's sociability and social preference behaviors by comparing these behaviors between WT and *Asic2*$^{-/-}$ mice. We measured these two social behaviors using a mouse social three-chamber test (fig. S4, A and B) and the mouse social preference test (fig. S4, D and E). Our findings did not reveal significant differences between the two groups in either of these behavioral tests (fig. S4, C and F). Moreover, the deletion of ASIC2 does not impair mechanosensation and hearing in mice (*36*). Collectively, these findings suggest that the increase of dominance in *Asic2*$^{-/-}$ mice may not be the result of elevated aggression, social interaction, or pain sensation loss.

To elucidate the potential behavioral mechanism through which *Asic2*$^{-/-}$ contributes to higher social dominance, we meticulously quantified the "effortful" behaviors during competition in the tube test (fig. S5A). As shown in previous studies, winner mice develop greater effortful behaviors, such as more approaches and push initiation in the tube test, and vice versa (*8*, *11*), implicating enhanced learning and memory involved in the formation of social dominance. This so-called "winner/loser effect," involving a memory mechanism, plays a crucial role in cost-benefit analysis during social competition, making winners more likely to win again and losers more likely to lose again (*8*, *11*, *37*, *38*). We quantified two key parameters of effortful behaviors, the number of pushes and retreats, in the tube test. Our findings indicate an increase in the number of pushes (fig. S5B) and a decline (fig. S5C) in retreats in *Asic2*$^{-/-}$ mice versus WT mice with or without the establishment of social dominance. These findings suggest that *Asic2*$^{-/-}$ winner mice demonstrate a more robust "winner effect" in comparison to both their WT littermates and the WT-winner mice in other groups. The outcomes provide a mechanism for interpreting how social dominance is formed, highlighting the crucial role of ASIC2 in regulating the learning and memory of effortful behaviors.

ASIC2 expression in the mPFC negatively correlates with social dominance

The mPFC plays a key role in social learning and memory and is also uniquely activated in the socially unstable dominance setting when viewing the superior compared to the inferior player (*39*, *40*). In rodents, the mPFC is involved in forming social dominance and the mPFC lesions lowered their social ranking relative to animals with an intact mPFC (*41*–*43*). ASIC2 is highly expressed in the mPFC, and other neuronal regions involved in social and emotional behaviors, such as the amygdala and thalamus (*33*, *44*–*46*). We isolated brain slices containing the mPFC and recorded acid-induced whole-cell currents in layer 5 pyramidal neurons of the PL subregion (Fig. 2A), which are primarily projection neurons in the mPFC. Gaining insight into their electrophysiological properties can illuminate the mechanisms underlying information transmission from the mPFC to downstream brain regions, thereby influencing behaviors. We found a robust ASIC-like current in WT neurons induced by low pH with a $pH_{50} = 6.2$ (Fig. 2B) and the current was diminished in neurons from *Asic1a*$^{-/-}$ mice (ASIC2-dependent currents) with a $pH_{50} = 4.2$ (Fig. 2C, note the unequal error bars). While neurons from *Asic2*$^{-/-}$ mice (homomeric ASIC1a-dependent currents) did not exhibit reduced current amplitude (Fig. 2, D to F), the current desensitization time was extended (Fig. 2, E to G), suggesting that total ASIC-conducted cation influx (e.g., Na^+ and Ca^{2+}) per unit time was increased in the neurons from *Asic2*$^{-/-}$ mice (Fig. 2H). Moreover, the pH_{50} in the neurons from *Asic2*$^{-/-}$ mice drifted from 6.2 to 6.4, suggesting a more sensitive pH response of ASICs than that in the WT neurons (Fig. 2, B to D). These data imply that the deletion of the ASIC2 subunit may fine-tune the sensitivity of ASIC channels to pH fluctuations within the synaptic physiological environment, considering that synaptic vesicle exocytosis reduces synaptic cleft pH by an estimated 0.2–0.6 units (*12*). Its presence ensures that knocking out the ASIC2 subunit enhances optimal responsiveness to physiological pH changes, thereby enhancing the regulation of synaptic transmission and neuronal excitability. To verify the absence of ASIC2 in *Asic2*$^{-/-}$ mice, we assessed mRNA and DNA levels in mPFC slices from both WT and *Asic2*$^{-/-}$ mice. Our data suggest a complete *Asic2* null in those brain regions (fig. S6, A and B). Moreover, after GluR blockade with AMPA and N-methyl-D-aspartate (NMDA) receptor (NMDAR) blockers, we detected GluR-independent EPSCs, which can be blocked by the ASIC inhibitor amiloride (200 μM), confirming the likelihood of the existence of functional ASIC-dependent EPSCs in the mPFC (fig. S6, C to E) (*12*, *47*).

To test whether ASIC2 is a part of the natural mechanisms essential for establishing social dominance, we detected the expression of ASIC1a and ASIC2 in the mPFC of a group of mice with stable linear ranking using Western blot analyses (Fig. 2I). Our data revealed a robust negative correlation between ASIC2 expression and social ranking in the tube test ($r = -0.80$, $P = 0.005$), while ASIC1a expression did not exhibit a significant correlation with social ranking ($r = -0.23$, $P = 0.18$) (Fig. 2, J to L). To further confirm the correlation between ASIC expression and social ranking, we

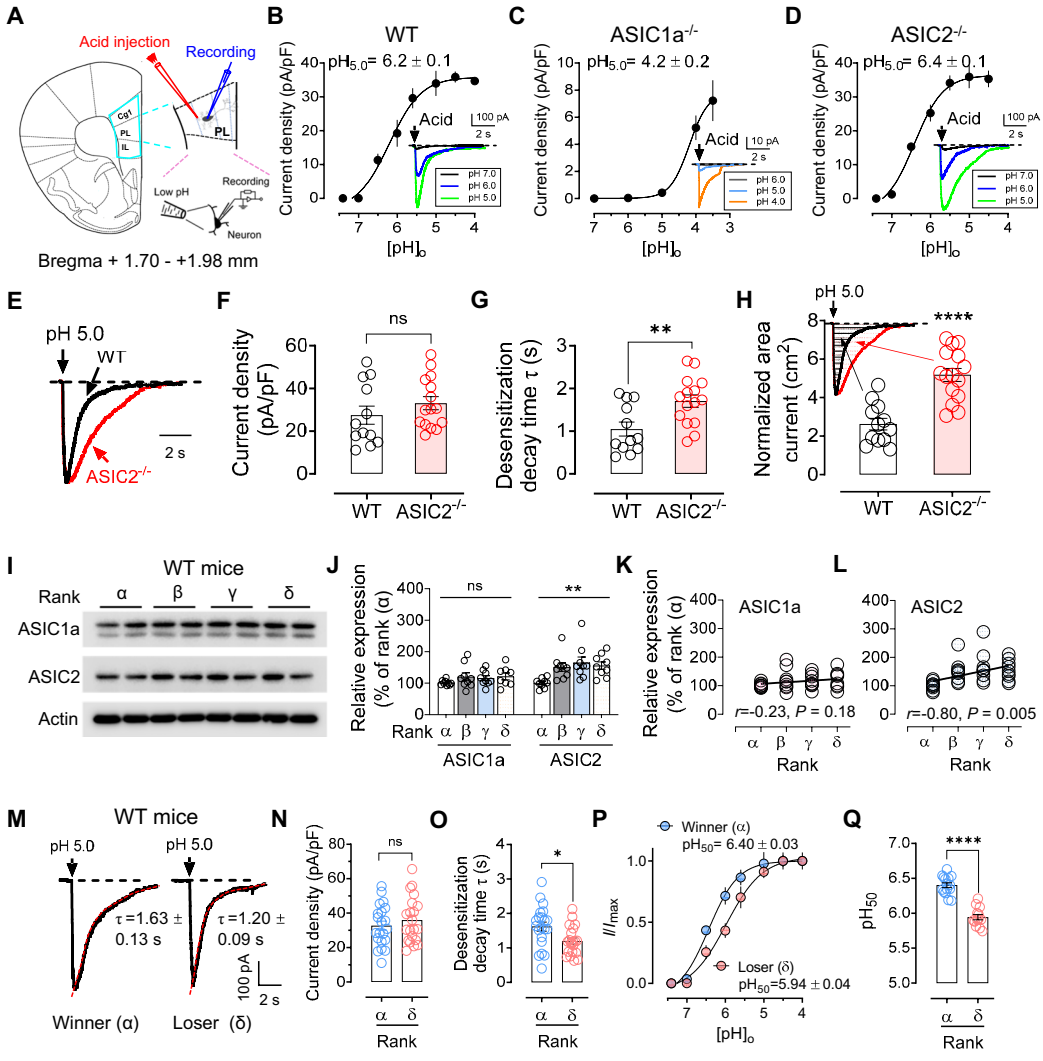

Fig. 2. Acid-induced ASIC-like currents in the mPFC correlate with social ranking. (**A**) Recordings of acid-induced currents in the mPFC slice. (**B** to **D**) pH-dependent ASIC currents in WT (B) ($n = 5$ to 13 cells per pH dose, from four mice), *Asic1a*$^{-/-}$ (C) ($n = 5$ to 21 cells per pH dose, from four mice) and *Asic2*$^{-/-}$ (D) neurons ($n = 5$ to 12 cells per pH dose, from 4 mice). (**E**) Normalized ASIC currents in WT (black) and *Asic2*$^{-/-}$ (red) neurons. (**F**) Current density at pH 5.0 in WT and *Asic2*$^{-/-}$ neurons. ns, $P = 0.2828$. (**G**) Desensitization decay times (τ), $^{**}P = 0.0058$, $n = 16$ cells per four mice. (**H**) Normalized ASIC current per unit time. $^{****}P < 0.0001$, $n = 15$ cells per four mice. (**I**) Representative Western blot data illustrating the expression of ASIC1a and ASIC2 in WT mice with different rankings in the tube test. (**J**) Average expression data for ASIC1a and ASIC2. ns, $P = 0.1592$, $^{**}P < 0.007$. (**K** and **L**) Correlation curves depicting expressions of ASIC1a [Pearson correlation coefficient (r) = −0.23, $P = 0.18$, ns] and ASIC2 ($r = -0.80$, $^{**}P = 0.005$) in relation to social rankings, $n = 9$ mice in each ranking group. (**M**) Representative ASIC currents in neurons from winner (α) and loser (δ) mice. (**N** and **O**) Average current density and τ of ASIC currents. ns, $P = 0.4211$; $^{*}P = 0.0113$, $n = 21$ cells per four mice. (**P**) pH-dependent ASIC currents in WT mice were analyzed to determine pH_{50} values, obtained by best-fitting with the Hill equation. (**Q**) Average pH_{50} between neurons in α and δ mice. $^{****}P < 0.0001$, $n = 13$ to 15 cells per four mice.

conducted additional measurements of ASIC currents in WT mice with established stable rankings (Fig. 2M). Upon comparing the characteristics of the ASIC currents, we found that the acid-induced current density in mPFC neurons from both the α (highest ranking) and δ (lowest ranking) mice did not exhibit any significant differences (Fig. 2N). However, the current desensitization time was significantly longer in mPFC neurons from the α mice compared to that in the δ mice (Fig. 2O). These interesting data suggest that the ASIC2 subunit may be less functional in the neurons of the winner mice compared to the loser mice, consistent with our above expression data in Fig. 2 (J to L). In addition, the pH dose-dependent curve of ASIC currents in the neurons from the winner mice is more sensitive than that in the neurons from the loser mice (Fig. 2, P and Q), also consistent with the data above showing the data of the higher pH_{50} in the *Asic2*$^{-/-}$ neurons than the WT neurons (Fig. 2, B to D). Altogether, these results suggest that functional ASIC2 is expressed in the mPFC and negatively correlates with social dominance behaviors in mice.

Rescuing ASIC2 in the mPFC decreases the social ranking

To examine whether restoring mouse ASIC2 (mASIC2) in the *Asic2*$^{-/-}$ mice can reverse the social ranking due to the deletion of ASIC2, we injected AAV_2-CMV-mASIC2-enhanced green fluorescent protein (EGFP) into the mPFC of the *Asic2*$^{-/-}$ mice (Fig. 3A).

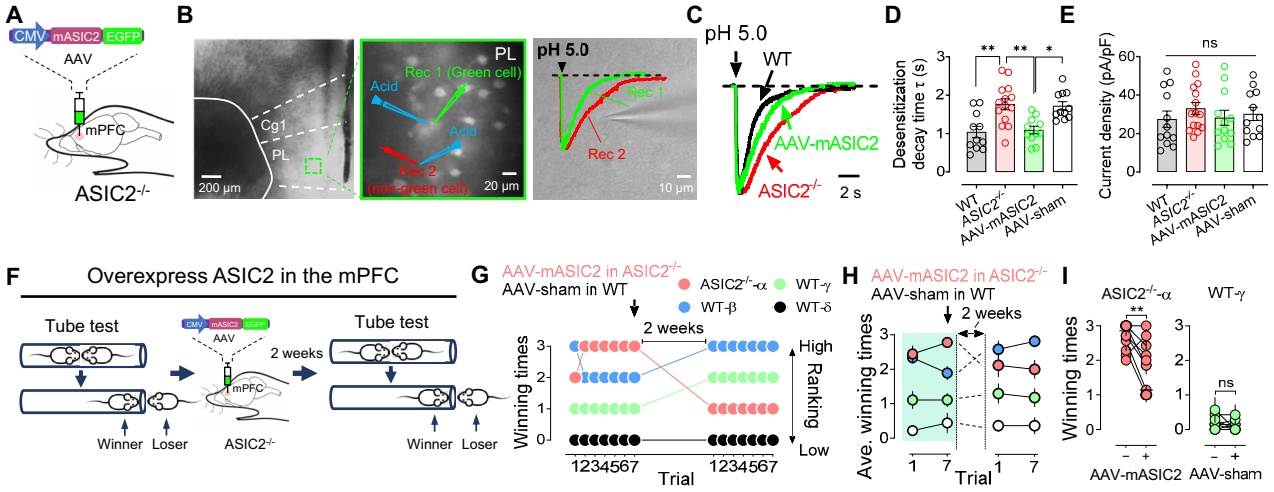

Fig. 3. Restoration of ASIC2 in the mPFC of *Asic2*$^{-/-}$ mice decreased social ranking. (**A**) Schematic showing the injection of AAV$_2$-CMV-mASIC2 into the mPFC in *Asic2*$^{-/-}$ mice. (**B**) Left, a representative image of the AAV$_2$-mASIC2 injection site and neurons expressing mASIC2; middle-right, representative recording of acid-induced ASIC-like currents in the GFP positive and negative neurons. (**C**) The representative comparison of acid-induced currents among WT, *Asic2*$^{-/-}$ (non-GFP cells), and AAV-mASIC2 neurons (GFP positive cells). (**D** and **E**) Comparison of desensitization decay times (D) and density (E) of the acid-induced currents in the neurons in (C). WT versus *Asic2*$^{-/-}$, $^{**}P = 0.0012$, *Asic2*$^{-/-}$ versus AAV-mASIC2, $^{**}P = 0.0082$; AAV-mASIC2 versus AAV-sham, $^{*}P = 0.0129$, ns, $P = 0.6763$, one-way ANOVA. $n = 12$ to 15 cells from four mice. (**F**) Schematic showing the tube test protocol before and after AAV-mediated expression of ASIC2 in the mPFC of *Asic2*$^{-/-}$ mice. (**G**) Representative result of ranking in the tube test following the restoration of ASIC2 in mPFC neurons of *Asic2*$^{-/-}$ mice. (**H**) Average winning times in the tube test after restoring ASIC2 in mPFC neurons of *Asic2*$^{-/-}$ mice. (**I**) Comparison of winning times between the group with restored ASIC2 in *Asic2*$^{-/-}$ mice and one of its WT subordinates. $^{**}P = 0.0092$; ns, $P = 0.3652$, two-tailed unpaired Student's *t* test. $n = 9$ cages.

Two weeks later, we recorded pH 5.0 acid-induced ASIC currents in the EGFP-expressing neurons (with nongreen cells as controls) of the PL subregion to evaluate the expression efficiency of ASIC2 (Fig. 3B). Currents in the PL subregion of the mPFC slices from the sham AAV group without mASIC2 were measured as another control. Our results confirmed the return of ASIC2 in the mPFC neurons, based on the restored desensitization times in ASICs (Fig. 3, C and D). The ASIC2 restoration did not increase the density of the ASIC currents induced by pH 5.0 (Fig. 3E). To examine whether restoring ASIC2 in the *Asic2*$^{-/-}$ mice can reverse the social ranking, we bilaterally injected AAV$_2$-CMV-mASIC2-EGFP into the mPFC of the *Asic2*$^{-/-}$ mice (α) in a stable ranking group, while its three WT subordinate cagemates received sham AAV particles. Two weeks later, the ASIC2-restored mice were subjected to the tube test to re-evaluate their social rankings (Fig. 3F). Our data indicate that transiently revitalizing ASIC2 expression in the bilateral mPFC of the *Asic2*$^{-/-}$ mice caused their tube test rank to descend, while the sham vector did not affect the ranking of the WT mice (Fig. 3, G to I, $n = 9$ cages), supporting the hypothesis that ASIC2 might contribute to the formation of social dominance.

ASIC2 regulates synaptic transmission in the context of social dominance

We began to evaluate synaptic transmission by testing the paired-pulse ratio (PPR) of EPSCs (Fig. 4, A to D). The PPRs in mPFC neurons did not show differences between WT and *Asic2*$^{-/-}$ mice (Fig. 4B). After 2 weeks of cohabitation, the PPRs in mPFC neurons of the winner mice were significantly smaller than that in the loser mice after the establishment of social dominance, suggesting an increase of presynaptic vesicle release in mPFC neurons of the winner mice (Fig. 4C). Notably, these differences are even more marked between the *Asic2*$^{-/-}$ winner mice and their WT subordinates (Fig. 4D).

We then tested whether ASIC2 regulates AMPAR-dependent synaptic transmission and plasticity in the context of social dominance. Previous studies described greater EPSCs in postsynaptic neurons after an equivalent presynaptic stimulation in dominant mice (*7*–*9*). Our AMPAR to NMDAR ratio data in mPFC pyramidal neurons suggest that the relative contributions of AMPAR and NMDAR are altered in *Asic2*$^{-/-}$ mice after the social dominance is established (Fig. 4, E and F). To further confirm whether ASIC2 regulates synaptic strength in establishing social dominance, we compared the mEPSCs in the WT and *Asic2*$^{-/-}$ mice "before hierarchy" and "after hierarchy" groups. The mEPSC amplitude in neurons from the WT winner mice was larger than that in the loser neurons, while the frequency exhibited no significant difference between the winner and loser groups (Fig. 4G). These observations suggest that the formation of social dominance is likely influenced by postsynaptic mechanisms. Notably, both the amplitude and frequency of the mEPSCs were enhanced in *Asic2*$^{-/-}$ winner neurons compared to their WT loser counterparts (Fig. 4H).

Building upon evidence that Ca^{2+}-permeable AMPARs (CP-AMPARs) play a key role in regulating homeostatic synaptic transmission and plasticity (*48*), we compared CP-AMPAR activity in WT and *Asic2*$^{-/-}$ neurons to elucidate the role of ASIC2 in regulating CP-AMPAR function. We first compared the CP-AMPAR–dependent EPSCs in WT and *Asic2*$^{-/-}$ neurons before the establishment of social dominance. Our data showed that the current rectification of AMPARs, one of the characteristics of CP-AMPARs (*49*), does not show a difference between WT and *Asic2*$^{-/-}$ neurons (Fig. 4I). Furthermore, we observed no discernible changes in the 1-naphthylacetyl spermine (NASPM, CP-AMPAR inhibitor)–sensitive EPSCs in the *Asic2*$^{-/-}$ neurons (Fig. 4L). These findings suggest that the deletion of ASIC2 does not alter the basal expression levels of CP-AMPARs in mPFC neurons. We then tested the CP-AMPAR–dependent EPSCs

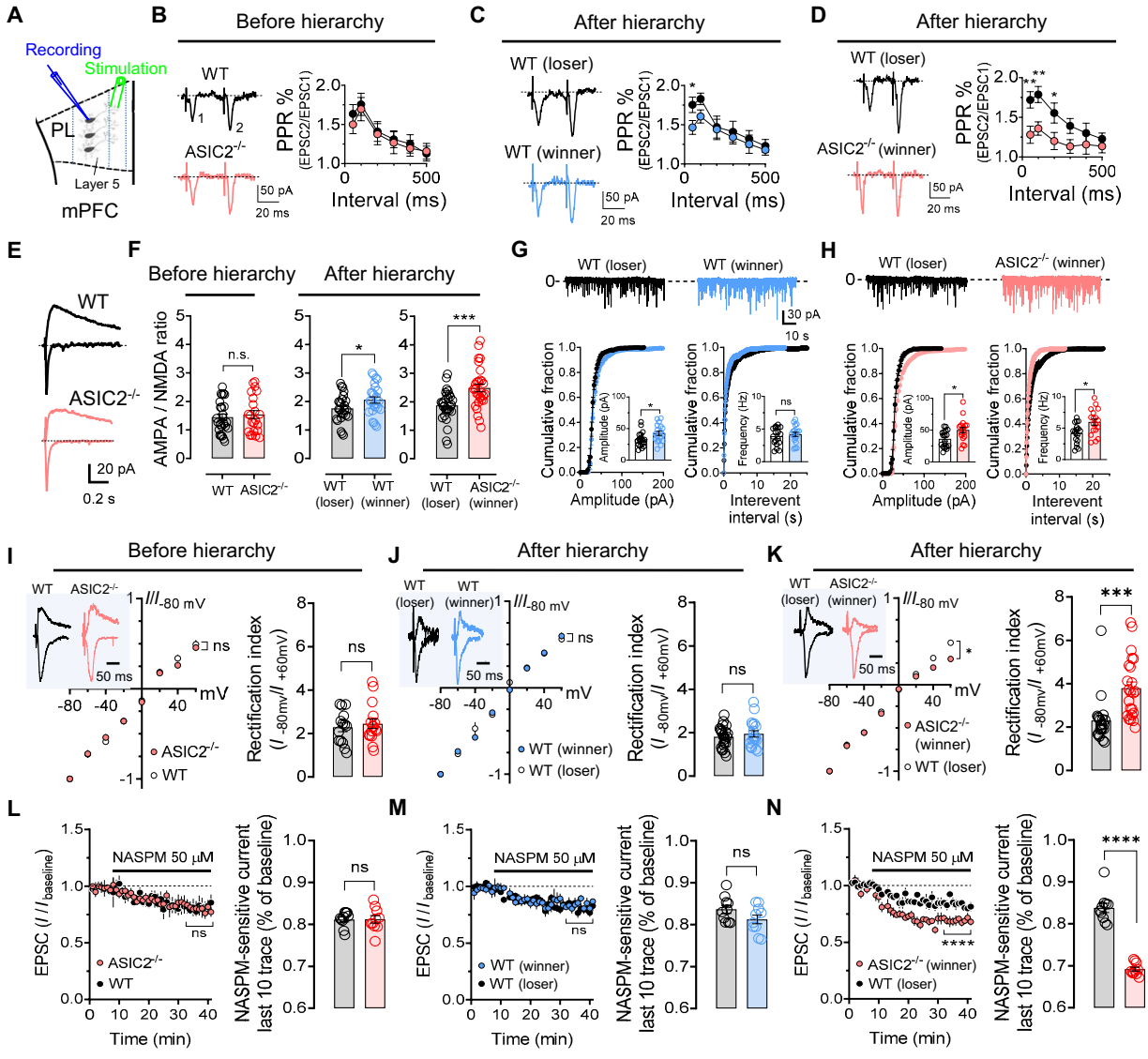

Fig. 4. Deletion of ASIC2 enhances synaptic transmission in social dominance. (**A**) Recording site schematic in the mPFC. (**B** to **D**) PPR recorded with 50- to 500-ms interstimulus intervals. Left: Representative PPR traces at 50 ms in WT and *Asic2*$^{-/-}$ mice before and after social rankings. Right: Average PPR plotted against intervals. (C) *$P = 0.0433$; (D) **$P = 0.0088$, 0.0044, *$P = 0.0481$, $n = 10$ cells per four mice. (**E**) Representative AMPAR-EPSCs (−80 mV) and NMDAR-EPSCs (+60 mV) in WT and *Asic2*$^{-/-}$ neurons. (**F**) Average AMPAR/NMDAR ratios before and after social rankings. Current amplitudes measured 70 ms after onset. ns, $P = 0.6117$; *$P = 0.0470$; ***$P = 0.0006$. $n = 22$ to 29 cells per five mice. (**G** and **H**) mEPSCs in the groups of WT versus WT, and WT versus *Asic2*$^{-/-}$ mice after social rankings. Upper: Representative mEPSC traces. Lower: Cumulative distributions of mEPSC amplitudes and interevent intervals. (G) *$P = 0.0342$; ns, $P = 0.4768$; (H) *$P = 0.0109$, 0.0065, $n = 18$ cells per four mice. (**I**) AMPAR current rectification in WT and *Asic2*$^{-/-}$ neurons before social rankings. Left: Current-voltage relationships of AMPARs. Inset: Representative AMPAR-EPSC traces at −80 mV and +60 mV. NMDARs blocked with 100 μM D-APV. Right: AMPAR current rectification index (−80 mV/+60 mV). ns, $P = 0.5913$. $n = 18$ cells per four mice. (**J** and **K**) AMPAR current rectification of WT versus WT, and WT versus *Asic2*$^{-/-}$ neurons after social rankings. ns, $P = 0.4467$; ***$P = 0.0003$, $n = 22$ cells per four mice. (**L** to **N**) Time course of 50 μM NASPM effect on EPSCs in mPFC neurons of WT versus WT (M) and *Asic2*$^{-/-}$ versus WT (N) mice groups before (L) and after (M and N) social rankings. NMDARs blocked with 100 μM D-APV. Right: NASPM-sensitive EPSC comparison. ns, $P = 0.9864$, $P = 0.1059$; ****$P < 0.0001$, $n = 10$ cells per four mice. All comparisons by two-tailed unpaired Student's *t* test.

after the establishment of a stable ranking in a group of WT mice. There were no changes in current rectification and NASPM-sensitive EPSCs in mPFC neurons from the winner mice (Fig. 4, J and M). Unexpectedly, we found strong current rectification and NASPM-sensitive EPSCs in the *Asic2*$^{-/-}$ neurons after hierarchy compared to the neurons in the WT subordinates (Fig. 4, K and N), suggesting the involvement of CP-AMPARs in *Asic2*$^{-/-}$-dependent social dominance.

To examine whether the loss of ASIC2 affects postsynaptic density protein 95 (PSD-95), a pivotal postsynaptic scaffolding protein in excitatory neurons (*50*), we compared the relative expression levels of PSD95 in the mPFC of *Asic2*$^{-/-}$ and WT mice before and after stable social hierarchy. Before the establishment of social hierarchy, there was no difference in PSD95 expression levels in mPFC tissue from *Asic2*$^{-/-}$ and WT mice (fig. S7A). We

found similar results in WT winner and loser mice with a stable social hierarchy (fig. S7B). However, PSD95 expression was substantially higher in the mPFC of *Asic2*$^{-/-}$-winner mice after social hierarchy than in their WT subordinates (fig. S7C). Overall, these findings suggest that the deletion of ASIC2 in the mPFC enhances synaptic activity in the context of social dominance behaviors through increasing PSD95 expression and CP-AMPAR–dependent neuronal activity.

ASIC2 regulates synaptic plasticity in the context of social dominance

A stable social dominance is determined by a two-stage mechanism. The initial ranking is achieved after a social encounter followed by facilitating a long-term memory to maintain the stability of the established dominance (*51*–*53*). Here, we further tested whether ASIC2 plays a role in regulating synaptic plasticity associated with social dominance. We compared LTP in *Asic2*$^{-/-}$-winner (α) and WT-loser (δ) mice with WT-winner (α) and WT-loser (δ) mice as controls (fig. S8A). We applied a high-frequency stimulation (HFS, 100 Hz, 1 s) to layer 2/3 and recorded the field excitatory postsynaptic potentials (EPSPs) in layer 5 of the mPFC PL subregion (fig. S8A). We found robust LTPs in the mPFC slices induced by the HFS from both winner and loser mice, and the LTP is more robust in the winner group (fig. S8, B and D). These data suggest stronger synaptic plasticity in the winner mice. We then recorded LTP in a group of mice consisting of one *Asic2*$^{-/-}$ winner mouse and one WT loser mouse. We found that LTP was further increased in *Asic2*$^{-/-}$ mPFC slices compared to both its WT subordinates and the WT winners in the control groups (fig. S8, C and D). ASICs are Na^+-selective cation channels permeable to Na^+ and/or Ca^{2+} ions (*16*, *54*). Activation of ASICs can conduct Ca^{2+} influx, directly contributing to LTP, or depolarize neurons via Na^+ influx, subsequently activating Ca^{2+} influx through CP-AMPARs and NMDARs (*12*, *29*, *55*). Regardless of whether ASICs directly induce the enhancement of LTP, these data suggest that the deletion of ASIC2, which can enhance the activity of ASICs (see Fig. 2, E to H), may exert a direct or indirect positive regulatory effect on LTP within the mPFC in the context of social dominance.

We then examined the effects of ASIC2 on the dendritic branches and spine morphology. Dendritic morphology has been widely indicated in the mechanism of synaptic plasticity (*56*–*58*). We housed a group of two WT male mice together for 2 weeks and subjected them to the tube test to confirm the social dominance. The slices containing mPFC were then dissected and fixed and the neurons in layer 5 of the mPFC PL subregion were filled with Alexa 568 through a patch-clamp pipette to image the dendritic branches and spine structure, density, and morphology (Fig. 5A). Using Sholl analysis, we determined the dendritic complexity by examining the branching numbers, branch length, and branch nodes (Fig. 5B) (*59*, *60*). Our data suggest that the animals with higher ranking display a more complex branching structure than their subordinates (Fig. 5C). The most notable changes were within 20 to 80 μm of the soma, with significant increases in the number of intersections (Fig. 5D) and branch points (Fig. 5E), but not in the numbers of nodes and the length of branches (Fig. 5, F and G). The *Asic2*$^{-/-}$-winner mice with higher ranking showed more significant increases in the number of intersections, branch points, numbers of nodes, and the length of branches (Fig. 5, H to L).

We further examined the morphology of dendritic spines in the context of social dominance. Although the total numbers of spines in the neurons of the winner mice are the same as their subordinates, we found variations in spine subtypes with increased numbers of mature spines and decreased immature spines in the neurons of the winner mice than that in the loser mice after the formation of social dominance (Fig. 5, M and N). Thus, we analyzed spine subtypes. Mature spines—most of which display "mushroom-like" morphology—have more stable postsynaptic structures enriched in AMPARs and are considered functional spines. In contrast, immature spines (thin, stubby, and filopodia) are unstable postsynaptic structures that have transitional ability. Immature dendritic spines are thought to be responsible for representing their ability for future synaptic plasticity, i.e., to develop into mature spines or disappear from the dendrite (*61*). The categories of spines were identified based on the parameters in the previous studies (refer to the details in Materials and Methods) (*56*, *62*). We found slightly decreased stubby and thin spines in the neurons in the winner mice (Fig. 5O). In addition, the ratio of mature to immature spines is higher in the neurons of the winner mice compared to the neurons of the loser mice (Fig. 5P). We compared the dendritic morphology in the neurons from the *Asic2*$^{-/-}$ mice with their WT subordinates. Notably, the total numbers of the spines are significantly increased in the neurons from the *Asic2*$^{-/-}$ mice than in their WT subordinates (Fig. 5, Q and R). Among these changes, the mature spines were significantly increased whereas the immature spines (thin spines) were significantly decreased (Fig. 5, R and S). The ratio of mature to immature spines is much higher in the neurons of the *Asic2*$^{-/-}$-winner mice (Fig. 5T). Combining the LTP and dendritic morphology data, our findings suggest that the deletion of ASIC2 may contribute to the enhancement of synaptic plasticity in mPFC neurons within the context of social dominance.

Identify the kinase pathways involved in ASIC2-dependent social dominance

We hypothesize that activation of postsynaptic ASICs triggers Ca^{2+}-dependent postsynaptic signaling pathways, resulting in the alternation of synaptic strength in response to social dominance change. Protein kinases are essential signaling components involved in various neuronal functions (*63*, *64*). To investigate the potential impact on kinase activities resulting from the deletion of ASIC2, mPFC tissue from *Asic2*$^{-/-}$ and WT mice after the establishment of the stable social ranking were subjected to kinome analysis using a serine/threonine kinase (STK) PamChip array. To identify STK families that may vary with social ranking change in *Asic2*$^{-/-}$ and WT mice, we created a heatmap using data from PamGene substrate phosphorylation events (Fig. 6A), and the quantitative analysis of individual peptide phosphorylation revealed a substantial difference in peptide phosphorylation patterns between the *Asic2*$^{-/-}$ and WT groups (Fig. 6B). The comprehensive kinase analysis using the kinome array suggests the potential STKs that were most likely responsible for the increased phosphorylation of the reporter peptides detected in the *Asic2*$^{-/-}$ mouse mPFC sample. Using three different thresholds for peptide selection, several kinases, including PKA and AKT, were identified, and their presence was considered not by random chance alone in the comparison between *Asic2*$^{-/-}$ and WT tissue samples. The presence of PKA and AKT predicted by peptides selected at a log2 fold change (LFC) cutoff of 0.3 was also significant (Fig. 6C). To identify changes in

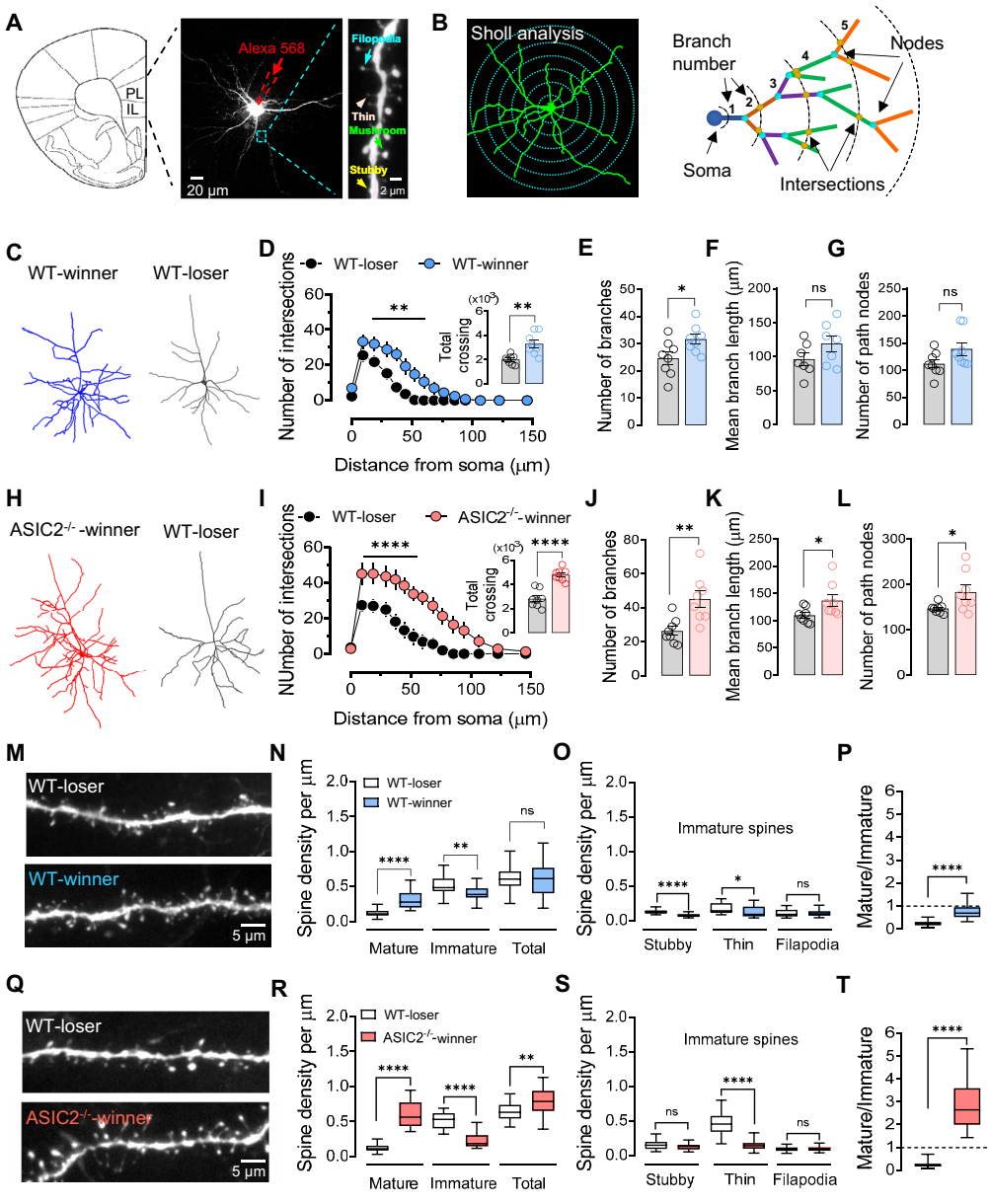

Fig. 5. Deletion of ASIC2 fosters dendrite and spine remodeling in social dominance. (**A**) Dendritic and spine morphology of mPFC neurons using Alexa 568 dye. (**B**) Sholl analysis for dendritic branches. Left: Parameters measured with Sholl shells from the cell body. Right: Nodes (blue dots) are branching points, and intersections (yellow dots) are where processes intersect Sholl shells. (**C**) Reconstructed mPFC neurons from WT winner and loser mice. (**D** to **G**) Sholl analysis of dendritic intersections (D), $^{**}P = 0.0019$; number of branches (E), $^{*}P = 0.0314$; branch length (F), ns, $P = 0.1465$; and node numbers (G), ns, $P = 0.0717$. $n = 6$ to 8 slices per four mice. (**H**) Reconstructed mPFC neurons from *Asic2*$^{-/-}$ winner and WT loser mice. (**I** to **L**) Sholl analysis: dendritic intersections (I) $^{****}P < 0.0001$; branches (J) $^{**}P = 0.0042$; branch length (K) $^{*}P = 0.0409$; and nodes (L) $^{*}P = 0.0412$. $n = 6$ to 8 slices per four mice. (**M**) Spine structures in mPFC neurons from WT winner and loser mice. (**N**) Spine density comparison: mature, $^{****}P < 0.0001$; immature, $^{**}P = 0.001$; total spines, ns, $P = 0.7656$. (**O**) Immature spine density (stubby, thin, and filopodia) in WT winner and loser mice. $^{****}P < 0.0001$; $^{*}P = 0.0253$; ns, $P = 0.9336$. (**P**) Mature-to-immature spine density ratio in WT winner and loser mice, $^{****}P < 0.0001$. $n = 27$ to 37 neurons per four mice. (**Q**) Spine structures in mPFC neurons from *Asic2*$^{-/-}$ winner and WT loser mice. (**R**) Spine density comparison: mature, $^{****}P < 0.0001$; immature, $^{****}P < 0.0001$; total spines, $^{**}P = 0.0026$. (**S**) Immature spine density in *Asic2*$^{-/-}$ winner and WT loser mice, $^{****}P < 0.0001$; ns, $P = 0.0624$, 0.6637. (**T**) Mature-to-immature spine density ratio in *Asic2*$^{-/-}$ winner and WT loser mice, $^{****}P < 0.0001$. $n = 27$ neurons per four mice. All comparisons by two-tailed unpaired Student's *t* test.

Asic2$^{-/-}$ regulation of protein kinases associated with social dominance behaviors, we compared kinase activities in WT and *Asic2*$^{-/-}$ mice that were not subjected to social hierarchy behaviors (fig. S9). Our data show the top protein kinase "hits" in WT versus *Asic2*$^{-/-}$ mice without social hierarchy behaviors, including BUD32, MST, MLCK, DYRK, and ERK. These top kinase hits differ in the WT and *Asic2*$^{-/-}$ mice after social hierarchy behaviors, which indicated that PKA, AKT, DMPK, PAKB, and MARK are dominant (Fig. 6, A to E).

ASICs-dependent Ca^{2+} influx was enhanced when ASIC2 expression was silenced, which was further supported by the observation that a group of Ca^{2+}-dependent kinases (e.g., PKA, AKT,

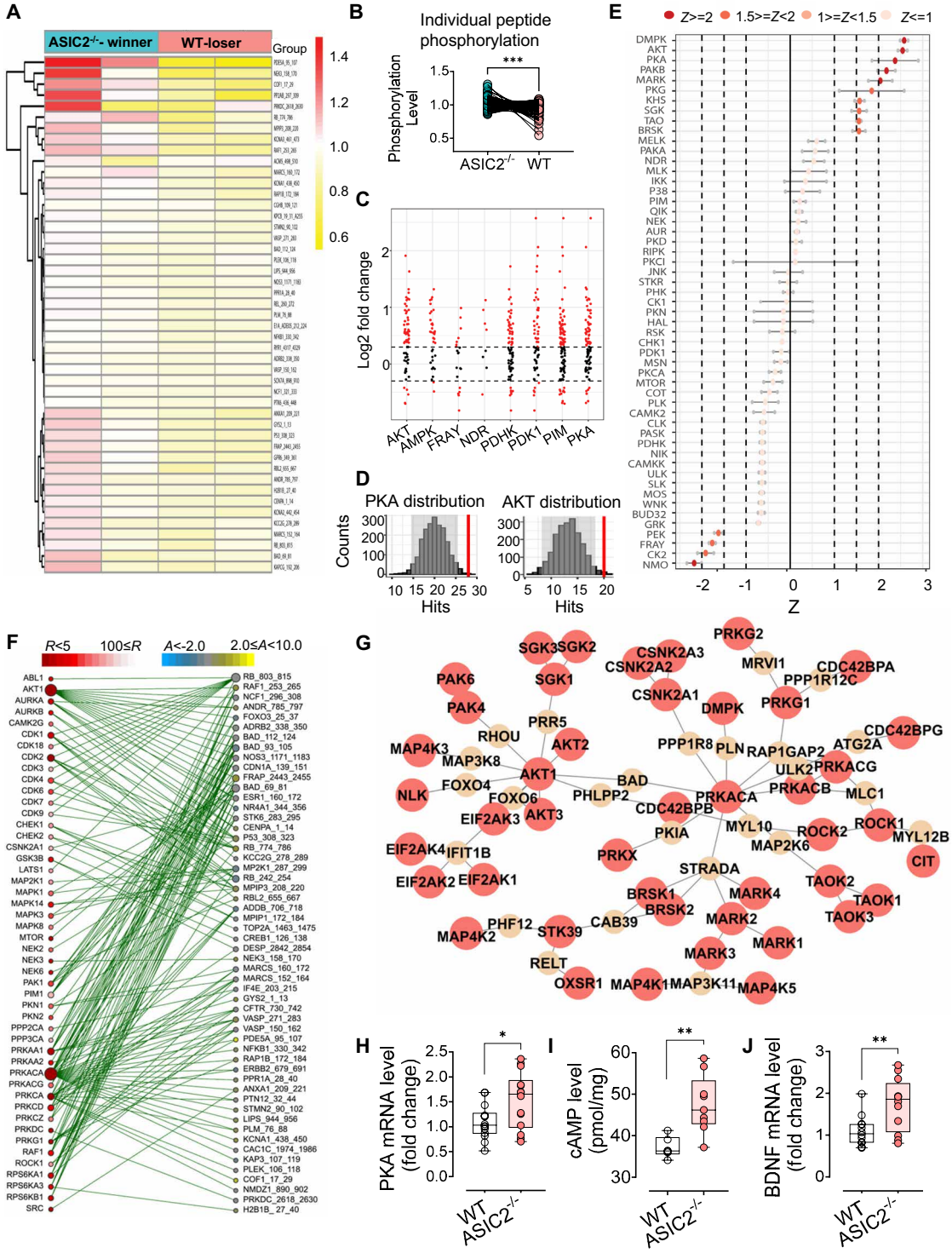

Fig. 6. Identifying ASIC2-dependent kinase pathways involved in social dominance. (**A**) Heatmap of substrate phosphorylation levels for STK in *Asic2*$^{-/-}$ brain samples versus WT controls. (**B**) Global phosphorylation level differences between *Asic2*$^{-/-}$ and WT brain samples. ***$P = 0.0001$ by paired two-tailed Student's *t* test. $n = 86$ peptides. (**C**) Reverse KRSA plots mapping peptides to upstream kinases in *Asic2*$^{-/-}$ versus WT brains. (**D**) Quantification of PKA and AKT ($Z > 2$) using histogram peacock plots. (**E**) Waterfall plot of differentially identified kinases in *Asic2*$^{-/-}$ brain samples versus WT controls. Red dots indicate increased or decreased representation for each kinase. (**F**) piNET analysis identified downstream proteins activated by STK pathways, highlighting PKA (PRKACA) and AKT1 pathways. Selected kinases (red nodes) and downstream regulators (blue nodes) are connected by green edges. (**G**) *Asic2*$^{-/-}$ molecular interaction network. Functionally enriched protein-protein interaction network of upstream kinase "hits" (red) and interpolated hidden nodes (yellow) identified by Kinograte R software. $n = 5$ mice per group. (**H**) mRNA expression of PKA (PRKACA) via RT-qPCR in *Asic2*$^{-/-}$ versus WT mice mPFC. *$P = 0.0217$ by unpaired two-tailed Student's *t* test. $n = 14$ mice per group. (**I**) Basal cAMP level measured by ELISA in *Asic2*$^{-/-}$ versus WT mice mPFC. **$P = 0.0039$ by unpaired two-tailed Student's *t* test. $n = 6$ to 9 mice per group. (**J**) mRNA expression of BDNF via RT-qPCR in *Asic2*$^{-/-}$ versus WT mice mPFC. **$P = 0.0062$ by unpaired two-tailed Student's *t* test. $n = 12$ mice per group.

AMPK, and PDK1) was notably activated in *Asic2*$^{-/-}$ mouse mPFC (Fig. 6C). The peacock plots for the PKA and AKT kinase families exhibited highly differential kinase activity (Fig. 6D) and data aggregation according to the STK family waterfall plot revealed that PKA and AKT were the most differentially active kinases of the Ca^{2+}-dependent kinases (Fig. 6E). We further analyzed downstream signaling pathways using piNET, a platform that can be used to annotate, map, and analyze a set of peptide moieties, including those with posttranslational modifications (*65*). The piNET data also showed a catalytic subunit of PKA (PRKACA) as the top predicted kinase hit (Fig. 6F). Subsequently, we assessed the kinase activity within a complex network of signaling pathways that occur in the *Asic2*$^{-/-}$ and WT groups, which identified three catalytic subunits of PKA (PRKACA, PRKACB, and PRKACG) as also involved (Fig. 6G).

We began by studying the PKA signaling pathway because the PKA signaling pathway is known to alter the functions of AMPARs by phosphorylation to regulate synaptic transmission and plasticity (*66*). Of course, we did not exclude other listed kinase pathways and will explore their potential roles in future studies (*67*, *68*). We found that the mRNA expression was significantly increased for PKA ($P = 0.0025$) in the *Asic2*$^{-/-}$ group (Fig. 6H). We then explored how the ASIC2-dependent PKA signaling regulates the upstream and downstream signaling pathways in social dominance behaviors. The basal cyclic adenosine monophosphate (cAMP) level measured by an enzyme-linked immunosorbent assay (ELISA) and brain-derived growth factor (BDNF) expression assessed by quantitative real-time polymerase chain reaction (RT-qPCR) analysis was higher in *Asic2*$^{-/-}$ mPFC than in WT samples (Fig. 6, I and J). These findings suggest a plausible mechanism by which ASIC2 loss in mPFC activates the cAMP-PKA-BDNF-PSD95 signaling pathway to enhance AMPAR functions, resulting in increased neuronal activity in the context of social dominance.

Deletion of ASIC2 in the mPFC alters synaptic excitatory/inhibitory balance

ASICs are widely expressed in both excitatory (*12*) and inhibitory neurons (*69*), suggesting that they might diversely affect neuronal functions. Although our data in Figs. 1 and 2 suggest the essential role of ASIC2 in the social dominance behaviors using the *Asic2*$^{-/-}$ mice, it is imperative to study the specific effects of ASIC2 on both excitatory and inhibitory neurons in the mPFC. We generated a global knockout (KO)–first-conditional KO (cKO)–ready mouse line to provide a rigorous comparison between global KO and cKO mice (fig. S10A). When crossed with a Cre mouse, a conventional ASIC2 KO mouse with GFP expression is produced. When crossed with a recombinase flippase (FLP) mouse, an *Asic2*-floxed (*Asic2*$^{f/f}$) mouse is produced. The conventional ASIC2 KO mice can be the controls of the cKO mice. For scientific rigor, we identified social ranking within four *Asic2*$^{f/f}$ mice and found a similar percentage of stable social ranking to that observed for WT mice (fig. S10B).

An AAV_2-hSyn-Cre-GFP was injected in mPFC in the *Asic2*$^{f/f}$ mouse to disrupt ASIC2 conditionally (Fig. 7A). All virus injection sites were verified histologically through the detection of GFP immunostaining (Fig. 7B and fig. S11, A and B). The immunofluorescence data suggest that ASIC2 expression is diminished in the AAV-hSyn-Cre–positive cells (Fig. 7C, lower) and the Western blot data confirmed that the expression of ASIC2 is decreased after the injection of AAV_2-hSyn-Cre (Fig. 7D). We then tested the effects of ASIC2 deletion by AAV_2-hSyn-Cre in the mPFC on social dominance behaviors. In brief, two *Asic2*$^{f/f}$ mice were housed for 2 weeks, and the ranking was determined by the tube test assay. The loser was bilaterally injected with AAV_2-hSyn-Cre into the mPFC, while the winner received sham AAV particles (AAV-hSyn-mCherry). Two weeks after the AAV injection, the mice underwent the tube test again to re-evaluate their rankings (Fig. 7E). We found that the deletion of ASIC2 by injecting AAV_2-hSyn-Cre into the mPFC neurons can reverse the social ranking (Fig. 7, F and G, $n = 9$ cages). We recorded the pH 5.0 acid-induced ASIC currents in the GFP-expressing neurons (with non-GFP cells as controls) of the mPFC PL subregion to evaluate the expression efficiency of AAV_2-hSyn-Cre. Our results confirmed the deletion of ASIC2 in the mPFC neurons, based on the extended current desensitization times in the ASIC-dependent currents (fig. S10C). To test whether ASIC2 deletion in the neurons alters the excitatory/inhibitory (E/I) balance, we examined the mEPSCs and mIPSCs to determine the E/I balance of the mPFC neurons. Twenty-four hours after the re-evaluation of ranking in the behavior protocol in Fig. 7E, mEPSCs and mIPSCs were measured in the acute brain slices of neurons in layer 5 of the mPFC PL subregion (Fig. 7, H and M). The ASIC2-cKO neurons (AAV-Cre) exhibited alternations of E/I balance relative to neurons from control mice (AAV-GFP/mCherry) with enhanced mEPSC amplitude and frequency (Fig. 7, I to L) and reduced mIPSC frequency (Fig. 7, N to Q), implicating a potential role of ASIC2 in regulating social dominance through enhancing the excitatory neuronal activity and perhaps decreasing the inhibitory neuronal activity in the mPFC.

Deletion of ASIC2 in the excitatory neurons, but not in the inhibitory neurons, in the mPFC alters social dominance behaviors

To study the effects of ASIC2 deletion in excitatory and inhibitory neurons specifically, we generated cell type–specific ASIC2 cKO mice lines by crossing the *Asic2*$^{f/f}$ mice with Vglut1-IRES2-Cre or Gad2-IRES-Cre transgenic mice (Fig. 8A and fig. S12A). The resulting homozygous ASIC2-Vglut1-cKO mice and ASIC2-Gad2-cKO mice were used to examine the effects of ASIC2 on the function of excitatory and inhibitory neurons, respectively. The Cre-positive neurons appeared with faint ASIC2 staining, suggesting an efficient ASIC2 cKO in both excitatory and inhibitory neurons (Fig. 8B and fig. S12B). For behavioral testing, one cKO mouse was housed together with three *Asic2*$^{f/f}$ cagemates for 2 weeks followed by determining the social ranking by the tube test. Our data suggest that the ASIC2-Vglut1-cKO mice were more dominant than their *Asic2*$^{f/f}$ cagemates (Fig. 8C, $n = 6$ cages) whereas the ASIC2-Gad2-cKO mice did not show significant dominance over their *Asic2*$^{f/f}$ cagemates (fig. S12C, $n = 6$ cages). More interestingly, we found that the ASIC2-Vglut1-cKO mice reached the stable ranking more rapidly than their *Asic2*$^{f/f}$ subordinates (Fig. 8D) whereas the ASIC2-Gad2-cKO mice showed a similar timescale with their *Asic2*$^{f/f}$ subordinates (fig. S12D).

To avoid potential developmental effects in transgenic mice, we disrupted ASIC2 in the mPFC excitatory and inhibitory neurons respectively using AAV_2-CaMKIIα-Cre (Addgene, no. 105558-AAV2/9) (Fig. 8E) and AAV_2-VGAT1-Cre (fig. S12E) (*70*). All AAV_2-CaMKIIα-Cre (Fig. 8F and fig. S11, C and D) and AAV_2-VGAT1-Cre (figs. S11, E and F, and S12F) virus injection sites were verified histologically. We then confirmed that the ASIC2 expression is diminished in the AAV_2-CaMKIIα-Cre and

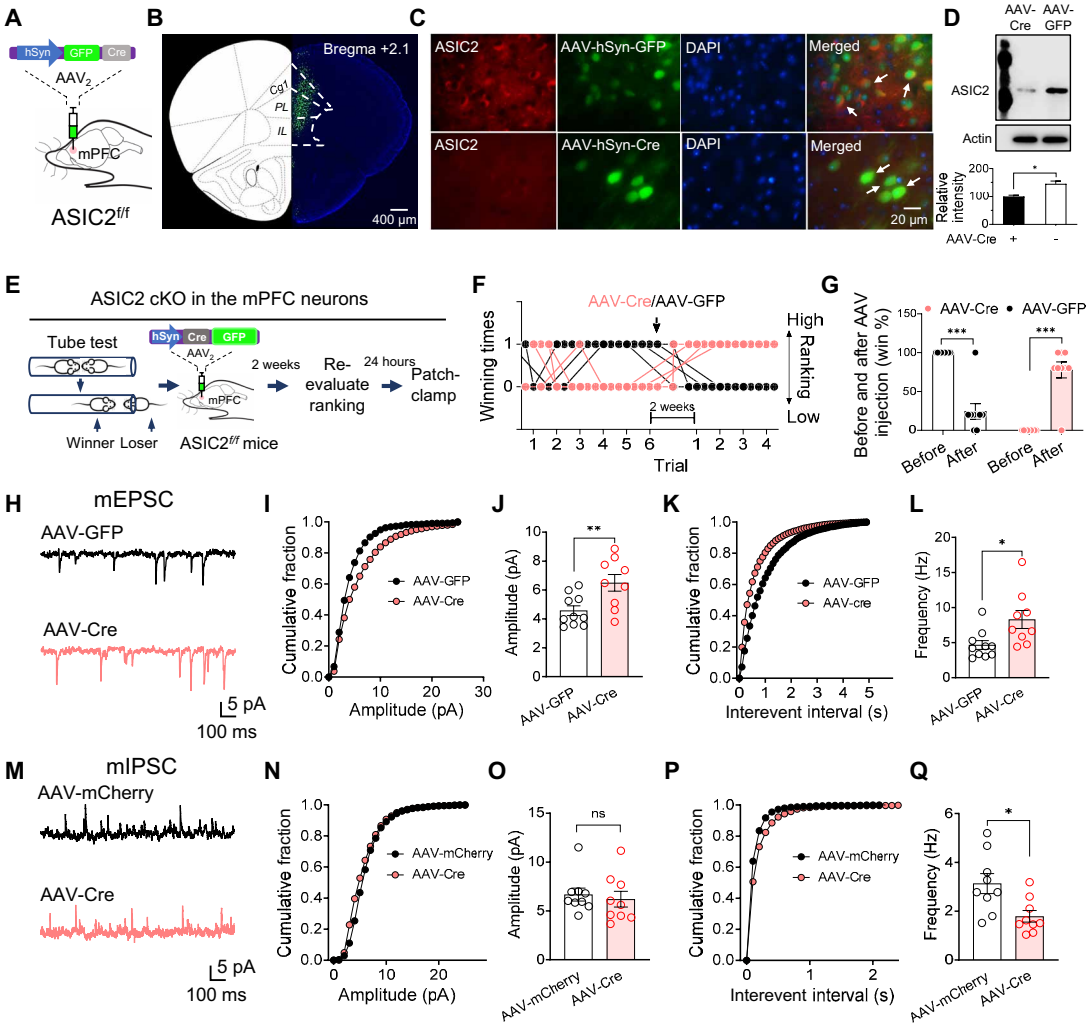

Fig. 7. Deletion of ASIC2 disrupts E/I Balance in mPFC neurons in the context of social dominance. (**A**) Schematic showing the AAV_2-hSyn-Cre injection into the mPFC of *Asic2*$^{f/f}$ mice. (**B**) Representative immunofluorescence image depicting the AAV_2-hSyn-Cre injection site. (**C**) Representative immunofluorescence image demonstrating colocalization of ASIC2 (red) and AAV_2-hSyn-Cre/AAV_2-hSyn-GFP (green). Please note the presence of colocalization indicated by arrows in the AAV_2-hSyn-GFP control group (upper), whereas such colocalization is absent in the AAV_2-hSyn-Cre group (lower). (**D**) Western blot results show ASIC2 protein levels in the AAV_2-hSyn-Cre and AAV_2-hSyn-GFP groups. $^*P = 0.0472$. $n = 6$ mice. (**E**) Schematic showing procedures of the tube test, AAV-hSyn-Cre injection into the mPFC of *Asic2*$^{f/f}$ mice, and the EPSC recordings. (**F**) Summarized results of ranking in the tube test before and after virus injections. (**G**) Average percentage of winning times in the tube test before and after AAV_2-hsyn-Cre and AAV_2-hSyn-GFP injections. $^{***}P = 0.0007$, $n = 9$ cages. (**H**) Representative mEPSC traces of *Asic2*$^{f/f}$ mPFC neurons in AAV_2-hsyn-Cre and AAV_2-hSyn-GFP groups. (**I** and **J**) Cumulative distributions of mEPSC amplitudes.$^*P = 0.0088$. (**K** and **L**) Cumulative distributions of mEPSC interevent intervals, $^*P = 0.0172$. $n = 10$ cells from four mice per group. (**M**) Representative mIPSC traces of *Asic2*$^{f/f}$ mPFC neurons in AAV_2-hsyn-Cre and AAV_2-hSyn-GFP groups. (**N** and **O**) Cumulative distributions of mIPSC amplitudes, ns, $P = 0.8873$. (**P** and **Q**) Cumulative distributions of mEPSC interevent intervals, $^*P = 0.0115$. $n = 9$ cells from four mice per group. All comparisons by two-tailed unpaired Student's *t* test.

AAV_2-VGAT1-Cre positive cells respectively through immunofluorescence (Fig. 8G and fig. S12G). We recorded the pH 5.0 acid-induced ASIC currents in the AAV_2-CaMKIIα-Cre and AAV_2-VGAT1-Cre neurons of the mPFC PL subregion to evaluate the expression efficiency of the Cre virus. Our results confirmed the deletion of ASIC2 in both AAV_2-CaMKIIα-Cre– and AAV_2-VGAT1-Cre–positive neurons, based on the extended current desensitization time of the ASIC-dependent currents (Fig. 8, H to J, and fig. S12, H to J). To evaluate how the AAV_2-CaMKIIα-Cre and AAV_2-VGAT1-Cre affect social dominance behavior, we first identified the social ranking within two *Asic2*$^{f/f}$ mice, followed by the Cre virus injection and social ranking re-evaluation in the tube test (Fig. 8K and fig. S12K). We found that the deletion of ASIC2 by injecting AAV_2-CaMKIIα-Cre into the mPFC neurons of the lower-ranking mice can raise the social ranking (Fig. 8, L and M, $n = 6$ cages). Similarly, we injected AAV_2-VGAT1-Cre into the mPFC of the higher-ranking or lower-ranking mice. However, no ranking changes were found in all groups (fig. S12, L and M, $n = 4$ cages). These data, altogether with the above data using the cKO mice, suggest a mechanism in which ASIC2 plays an important role in regulating the excitatory neuron rather than affecting the inhibitory neurons in the mPFC

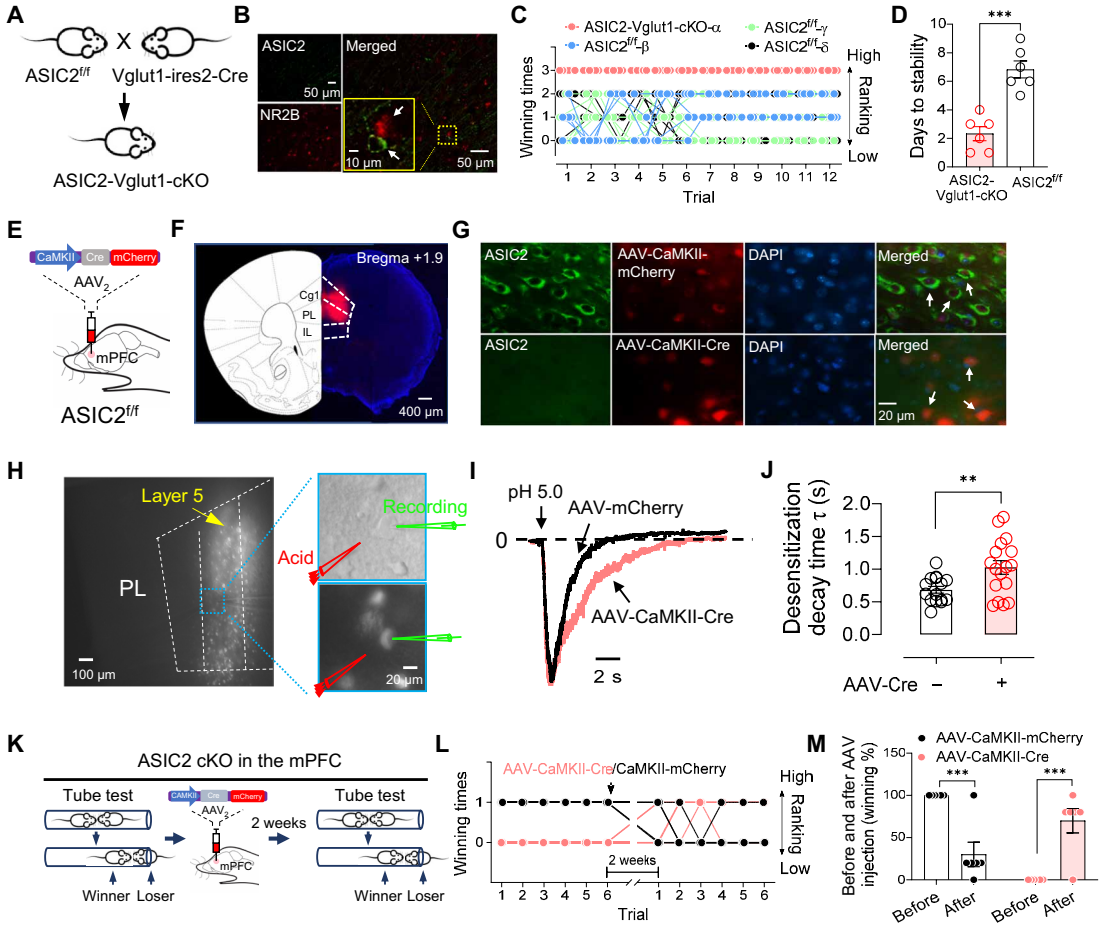

Fig. 8. Deletion of ASIC2 in mPFC excitatory neurons elevates social ranking in mice. (**A**) Generation of ASIC2-cKO mice in excitatory neurons (ASIC2-Vglut1-cKO) by crossbreeding *Asic2*$^{f/f}$ mice with Vglut1-ires2-Cre mice. (**B**) Immunofluorescence images showing the absence of ASIC2 expression (green) in mPFC excitatory neurons labeled with *N*-methyl D-aspartate receptor subtype 2B (NR2B) (red). Inset highlights the lack of ASIC2 and NR2B colocalization. (**C**) One ASIC2-Vglut1-cKO and three WT mice cohoused for 2 weeks, followed by the tube test tournament to establish social rankings. Data from six cages per group summarized. (**D**) Comparison of time to stable rankings between ASIC2-Vglut1-cKO and WT subordinate mice. ***$P = 0.0002$, $n = 6$ cages. (**E**) Schematic of AAV_2-CaMKIIα-Cre injection into *Asic2*$^{f/f}$ mouse mPFC neurons. (**F**) Representative image of AAV_2-CaMKIIα-Cre injection site. (**G**) Immunofluorescence image demonstrating ASIC2 (green) and AAV_2-CaMKIIα-Cre/mCherry (red) colocalization. Arrows indicate colocalization in AAV_2-CaMKIIα-mCherry, but not AAV_2-CaMKIIα-Cre group. (**H**) Whole-cell patch-clamp recording of acid-induced ASIC-like currents in AAV_2-CaMKIIα-Cre (mCherry positive) mPFC neurons. (**I**) Representative traces of acid-induced currents in AAV_2-CaMKIIα-Cre (red) and AAV_2-CaMKIIα-mCherry (black) neurons. (**J**) Comparison of desensitization decay times of acid-induced currents in neurons from (I). Effective ASIC2 deletion in AAV_2-CaMKIIα-Cre neurons shows prolonged desensitization times. **$P = 0.0082$. $n = 15$ to 17 cells from four mice per group. (**K**) Schematic of tube test procedures following AAV_2-CaMKIIα-Cre injection into *Asic2*$^{f/f}$ mouse mPFC. (**L**) Summary of tube test rankings before and after AAV_2-CaMKIIα-Cre and AAV_2-CaMKIIα-mCherry injections. (**M**) Average percentage of winning times in the tube test before and after AAV_2-CaMKIIα-Cre and AAV_2-CaMKIIα-mCherry injections. ***$P = 0.0007$, $n = 6$ cages. All comparisons by two-tailed unpaired Student's *t* test.

and support the conclusion that deletion of ASIC2 in the excitatory neurons dominantly regulates social dominance behaviors.

DISCUSSION

The enigma of social interactions and the consequent formation of social hierarchy have captivated scientists for many years. Our current research, which delves into the molecular intricacies of social dominance, underscores the intricate link between synaptic transmissions in the mPFC and the manifestation of dominance behaviors in mice. Spotlighting the integral function of ASIC2, this study illuminates previously unexplored facets of social dominance understanding. We reveal ASIC2 as a paramount regulator of mPFC neurons, directing the course of social dominance in mice. Its absence results in diminished stability in dominance patterns. The study further unravels the molecular strategies and pathways influenced by ASIC2 within the mPFC, emphasizing its pronounced effect on excitatory neurons and its consequential modulation of synaptic transmission and plasticity through the manipulation of GluR functions (fig. S13).

The formation of social dominance requires the remodeling of synaptic transmission and plasticity (*7*–*11*). While AMPARs are recognized as critical for social dominance behavior, the upstream or parallel regulators are poorly known. Revealing the regulators is important to understand the regulatory mechanisms of the formation of social dominance. For example, the expression and function of

AMPARs are elevated in the mice with top ranking and alterations in GluR4 expression correspondingly influence this ranking (*7*). Our research suggests that ASIC2 may be the direct upstream regulator of glutamatergic synaptic transmission. This assumption stems from our observations that *Asic2*$^{-/-}$ mice demonstrate a pronounced dominance phenotype in contrast to their WT counterparts, suggesting the role of ASIC2 in shaping social dominance behaviors through the modulation of glutamate synapse function (Fig. 1).

Another interesting question arises: Is ASIC2 essential for the establishment of social hierarchy? If so, one prediction is that the deletion of ASIC2 in mice may interrupt the process of establishing social hierarchy. We observed that *Asic2*$^{-/-}$ mice indeed exhibit decreased stability of social rankings within their groups compared to WT groups within 7 days of tube tests (fig. S1C and Fig. 1, B and E). All *Asic2*$^{-/-}$ mice tend to position themselves at higher rankings within a group. This inherent behavior of "high-ranking" *Asic2*$^{-/-}$ mice may disrupt or prolong the establishment of stable social rankings within a group.

The role of ASICs in modulating neuronal activity in the mPFC and its subsequent impact on social dominance behaviors raises intriguing questions. The brain's extracellular pH is very dynamic. Neural activity can induce transient and localized pH fluctuations (*12*, *15*, *71*). As social dominance forms, both winners and losers might experience shifts in neuronal activation, network remodeling, and neuronal metabolism that might cause micro-region pH fluctuation. Recent studies suggest that localized pH changes in conjunction with both pre- and postsynaptic ASICs might function as a signaling mechanism in neuronal communications. It is conceivable that changes in neuronal excitability and synaptic plasticity, hitherto solely attributed to intracellular Ca^{2+} transients, may include a notable component mediated by pH shift (*72*), and that H^+ may function as a neurotransmitter to affect these changes (*12*, *14*, *71*). Furthermore, our results indicate that ASIC1a and ASIC2 form heterozygous channels in mPFC neurons (Fig. 2). Thus, mPFC neurons have H^+-gated currents consistent with ASIC2/1a heteromeric channels and/or ASIC1a homomeric channels. While neurons from *Asic2*$^{-/-}$ mice did not exhibit reduced current, the desensitization time was extended (Fig. 2, E to G), suggesting that total ASIC-dependent cation influx (e.g., Na^+ and Ca^{2+}) per unit time was increased in the neurons from *Asic2*$^{-/-}$ mice (Fig. 2H), potentially leading to enhanced neuronal activity. Our findings suggest a foundational model of ASIC functions in the social dominance behaviors in the mPFC. Here, ASIC1a homomeric channels take precedence, while ASIC2 modulates the functions of ASIC1a. Activation of ASICs is known to stimulate neurons by increasing intracellular Na^+ or Ca^{2+} levels, which, in turn, amplifies AMPAR and NMDAR functions (*12*). Consistent with this, we observed amplified AMPAR and NMDAR functions in dominant *Asic2*$^{-/-}$ mice (Fig. 4).

To further understand the interplay between ASIC activation, synaptic transmission, and plasticity in the context of social dominance, we investigated the associated signaling pathways. A crucial consideration is the elevation of ASIC-dependent intracellular Ca^{2+} might activate the Ca^{2+}-dependent signaling pathways. Social dominance behaviors are mediated by serial neuronal transmission and plasticity processes, driven by a suite of kinases. They might modulate synaptic transmission by changing ion channel properties or concentrations or orchestrate protein synthesis, thereby altering synaptic structure and synaptogenesis. By mediating phosphorylation on target proteins, they alter these proteins' biochemical functions and influence the signal transduction processes they are engaged in (*9*, *44*, *73*). We used a protein kinase activity array to narrow down the candidates. We screened several Ca^{2+}-dependent kinases that were notably activated in the mPFC of *Asic2*$^{-/-}$ mice. We first focused on the PKA signaling pathway because it is well studied and known to alter the functions of AMPARs by phosphorylation and is highly associated with synaptic transmission and plasticity. The cross-talk between Ca^{2+} and cAMP/PKA signaling in regulating cell function has been appreciated for decades (*74*) and has since been expertly reviewed (*75*–*77*). The role of cAMP-dependent PKA in learning and memory was revealed by discovering the essential of PKA signaling in long-term memory by using contextual fear-conditioned animals (*78*, *79*) and by using inhibitors against PKA activity (*80*–*83*). In addition, cAMP-dependent PKA involves reward-related learning and social behaviors (*84*). Although the results imply the role of PKA in the mPFC of *Asic2*$^{-/-}$ mice versus WT mice in the context of social dominance, we posit that the cAMP-dependent PKA is not the only kinase involved in social dominance behaviors, and future research is warranted in this area.

We also identified the different roles of ASIC2 in excitatory and inhibitory neurons. While ASICs are expressed in different types of neurons including glutamatergic and GABAergic synapses, many studies regarding the roles of ASICs in synaptic transmission have focused on glutamatergic synapses (*85*). However, synaptic cleft acidification also occurs at inhibitory GABAergic synapses (*86*). Moreover, the selective deletion of ASIC1a in GABAergic neurons yields important functional consequences (*87*, *88*). Nevertheless, very few studies focused on the potential role of ASICs, especially ASIC2, on either glutamatergic or GABAergic synapses. This is largely due to the lack of an ASIC2 cKO mouse model. To address this gap, we generated an ASIC2 KO-first-cKO-ready mouse line for this study. The overall outcomes of the social dominance behaviors from the *Asic2*$^{-/-}$ mice suggest that the deletion of ASIC2 raised the social ranking. This outcome might come from the regulatory balance of ASIC2 in excitatory and inhibitory neurons. Our analyses of mEPSC and mIPSC suggest that ASIC2 deletion in mPFC neurons alters the E/I balance by changing both activities. However, it is important to note that only the deletion of ASIC2 in excitatory neurons changed social ranking. In contrast, the deletion in inhibitory neurons had no discernible impact. This implies that the targeted deletion of ASIC2 in excitatory neurons within the mPFC could be instrumental in regulating social dominance behaviors.

One limitation of this study is the absence of deeper exploration into the various mPFC ascending and descending circuitries. Multiple mPFC-dependent circuitries, including mediodorsal thalamus (MDT)–mPFC (*8*) and mPFC-lateral hypothalamus (LH) (*10*), have been implicated in the formation of social dominance and behaviors associated with social ranking. In addition, various other brain circuits, such as MDT–anterior cingulate area (ACC), MDT-hippocampus CA2, and ACC–nucleus accumbens, are involved in social dominance behaviors in both rodents and primates (*89*). However, the specific impact of ASIC2 deletions within these distinct circuits on social dominance remains entirely unexplored. Another limitation pertains to the specificity of the effects observed in the studied cell types lacking ASIC2. While we have delineated the distinct role of ASIC2 cKO in glutamatergic neurons as opposed to GABAergic neurons, it is important to note that this represents only a subset of neuronal populations. Subsequent studies should aim to

elucidate the precise function of *Asic2*$^{-/-}$ across diverse cell types, including neurons and glial cells, particularly within the brain circuits implicated in social dominance behaviors, as outlined above.

In summary, this study describes a molecular mechanism that ASIC2 regulates social dominance behaviors (fig. S13). The journey from molecular revelations to behavioral observations has been an enlightening one, expanding the horizons of our understanding of the neural mechanisms anchoring social dominance. The potential of ASIC2 and H^+ to serve as diagnostic biomarkers for social dominance circuits could proclaim an era of research. As we get closer to these breakthroughs, it is exciting to think about how these understandings could lead to better ways of treating common social problems like social cognitive deficits (*90*), depression, social anxiety, and posttraumatic stress disorder. The impact on society could be profound.

MATERIALS AND METHODS

Animals

We used both male and female mice 12 weeks of age. Mice were derived from a congenic C57BL/6 background including WT, *Asic1a*$^{-/-}$, *Asic2*$^{-/-}$, Vglut1-IRES2-Cre-D, Viaat-IRES-Cre, and Flp-recombinase. The *Asic1a*$^{-/-}$ and *Asic2*$^{-/-}$ mice were a gift from M. Welsh and J. Wemmie's laboratories at the University of Iowa and maintained in our animal facilities. The C57BL/6 (JAX, no. 000664), Vglut1-IRES2-Cre-D (JAX, no. 023527), Viaat-IRES-Cre (JAX, no. 010802), and Flp-recombinase (JAX, no. 031629) mice were ordered from the Jackson Laboratory and maintained in our animal facilities. The *Asic1a*$^{-/-}$ (JAX, no. 013733) and *Asic2*$^{-/-}$ (JAX, no. 013126) homozygous mice line was refreshed every 8 to 10 generations by backcrossing to the C57BL/6J mice. Nonlittermates generated from these crosses were used in behavioral assays. To ensure scientific rigor, experimental factors, such as sex, age, and weight are closely matched throughout the study (male mice, aged 12 weeks ± 4 days; weight, 25 ± 2.5 g; female mice, aged 12 weeks ± 4 days; weight, 20 ± 2.0 g). Experimental mice were maintained on a standard 12-hour light-dark cycle and received standard chow and water ad libitum. Animal care and procedures met the National Institutes of Health standards. The University of Tennessee Health Science Center Laboratory Animal Care Unit approved all procedures (protocol no. 19-0112).

Production of ASIC2 KO-first cKO-ready mice

Mice carrying a deletion of exons 2 of the *Asic2* gene flanked by *LoxP* sites were produced by Biocytogen (fig. S7). The *SA-P2A-EGFP-PA* cassette was eliminated by crossing these mice with Flp recombinase mice. The *SA-P2A-EGFP-PA* cassette-deleted *Asic2*$^{f/+}$ mice were crossed with Cre recombinase mice, and the resulting mice were then crossed with *Asic2*$^{+/+}$ mice to introduce the *Asic2* Δ*2* allele. On the other hand, when the ASIC2 KO-First cKO-Ready mice were crossed with Cre recombinase mice, the global KO mice with the *SA-P2A-EGFP-PA* cassette were produced. To generate ASIC2 cell type–specific cKO mice, homozygous *Asic2*$^{f/f}$ female mice were crossed with double-heterozygous Vglut1-Cre; *Asic2*$^{f/+}$ male mice or homozygous Gad2-IRES-Cre. The control group for the cKO mice was Cre-negative *Asic2*$^{f/f}$ nonlittermates. In all, this breeding strategy for the ASIC2 KO-First cKO-Ready mice can allow us to compare all global and cKO mouse lines in the same pure C57BL/6 background. Genotyping of global KO mice was performed using the following primers: for WT allele (350 bp): 5′-GAA GAG GAA GGG AGC CAT GAT GAC-3′ and 5′-AGT CCT GCA CGG TGG GAG CTT CTA-3′; for deletion (del) allele (450 bp): 5′-TGG ATG TGG ATT GTG TGC GA-3′ and 5′-ATG GTT TCG GAG TGG TTT GGC ATT GTG-3′. Genotypes of Vglut1-Cre; Asic2$^{f/f}$ mice were determined by PCR using the following primers: for floxed (515 bp) or WT allele (469 bp): 5′-GGG CAA GTA GAG GAG GCT ATG AGG T-3′ and 5′-ATG TGG ATC CCA TTT GTC TCT GGC T-3′; for Viaat-Cre allele (344 bp): 5′-ATG AGC GAG GAG AAG TGT GG-3′.

Behavioral tests

The protocols for each experiment are detailed in the schematics of each figure. All mice were handled by experimenters for 30 min on each of the 3 days before actual behavioral tests. Mice were then exposed to varying protocols, as described below.

Dominance tube test

The tube test protocol was modified from Wang *et al.* (*7*). In brief, a clear acrylic tube with a 30-cm length and a 2.8-cm inside diameter is used in which one mouse can pass or move backward through the tube easily but cannot make a U-turn or climb through another mouse. The mice underwent a 3-day training in which all mice went through the tube 10 times per day, 5 times from each side without another competitor in the tube. The training procedure allows the mice to adapt to the test procedure and environment. The mice, in a very rare case, cannot be trained and were excluded for further testing. In the testing procedure, tests were conducted in a pairwise style among cagemates using a round-robin design, and the number of times won by individual animals was recorded to determine the hierarchical ranking. The mouse who forced its competitor out of the tube was declared the "winner," or dominant in this situation. The mouse that was retreated is then designated the "loser," or subordinate. In most cases, the competition was completed within 2 min, or the tests were repeated. The rank is considered stable without ranking change in all mice for at least five consecutive days. Groups were categorized as "nonstable ranking" if they did not form a stable ranking within 2 weeks. From trial to trial, the mice were assigned at either end randomly. Within the group of four males, each mouse encountered every other mouse in the group only once, resulting in a total of six possible pairs in the tests. In a round-robin tube test tournament trial, each mouse competed against the other three mice individually, and winning times were recorded. The rankings were marked α, β, γ, and δ from high to low, according to their average winning times over seven trials. We housed one *Asic2*$^{-/-}$ male mouse together with three male WTs for 2 weeks and subjected all of them to a round-robin tube test tournament (one trial per day for 7 trials) to determine social ranking, the ranking of the *Asic2*$^{-/-}$ winner was marked *Asic2*$^{-/-}$-α, and the ranking of the three WT mice was marked WT-β, WT-γ, and WT-δ (rank from high to low), according to their average winning times of seven trials. In the three *Asic2*$^{-/-}$ and one WT group, the ranking of the three *Asic2*$^{-/-}$ mice was marked *Asic2*$^{-/-}$-α, *Asic2*$^{-/-}$-β, and *Asic2*$^{-/-}$-γ, as well as the loser WT-δ (rank from high to low), according to their average winning times of seven trials.

Warm spot test

The warm spot test protocol was modified from Zhou *et al.* (*8*). A group of mice was placed on an ice-cold floor with a warm spot in the corner, mimicking the natural competition over limited resources, and the ranking of social dominance was determined by the amount of time that each mouse occupied the warm spot. In brief, A

regular mouse cage (30 cm × 19 cm × 13 cm) was put on ice with a temperature <4°C. A round warm stage with temperature control to 30°C was placed at the corner of the cage. The diameter of the stage is 5 cm and allows the occupation of only one adult mouse. Four mice after 2 weeks of being cagemates and after determining social ranking after the tube test were placed in a cold cage without a warm stage for 30 min and then the warm stage in the cage was followed by videotaping the mice for 20 min. The time spent on the warm stage by each mouse was analyzed and used to determine the ranking among the four cagemates.

Urine marking test

For a cage of four male mice, we used a similar round-robin design in the tube test to evaluate the urine marking patterns (two pairs/day, total 3 days). The urine marking test protocol was modified from Wang *et al.* (*7*). In brief, a mouse cage (30 cm × 19 cm × 13 cm) was divided into two equal chambers by a wire mesh with filter papers on the bottom. In this paradigm, two cagemates were housed on opposite sides of the mesh-separated cage for 2 hours, urine marks were collected on the filter paper in the cage visualized under UV light, and the relative dominance between two mice was determined by assessing the number and size of the marks and their distance from the mesh.

Open field test

The open field task was used to determine the general activity levels, gross locomotor activity, and exploration habits of the mice. The assessment took place in a square, white plastic box (30 cm × 30 cm × 30 cm). Mice were placed in a corner of the arena and allowed to explore the new environment for a total of 10 min. Their movements were videotaped. The footage including the distance moved, velocity, rest time, movement time, and the time spent in the center and corner of the arena was analyzed using the ANY-maze software. This test provides us with an initial screen for locomotion and anxiety-related behavior (time spent in the center).

Three-chamber social test

Test mice were placed in an automated three-chamber apparatus (61 cm × 41 cm × 23 cm) (*91*). The test session began with a 10-min habituation session in the chamber with two empty wire cups in the left and right side. During the second 10 min, a novel mouse (stranger 1), previously habituated to the enclosure, was placed in an identical wire cup located in one side chamber. A small flowerpot in a wire cup (object) was placed in the other side chamber. Mice activities were detected by a camera positioned above the chamber. Subsequently, another novel stranger (stranger 2) was introduced under the empty cup, replacing the flowerpot, for a 10-min social novelty session. Mice activities were video recorded again. The time test mice spent within 2 cm of the wire cup was analyzed using the ANY-maze software. The social index was calculated by the ratio of time the test mouse spent with the object versus stranger 1 and stranger 1 versus stranger 2.

Social partition (preference) test

A standard cage (61 cm × 41 cm × 23 cm) was divided in half by a perforated partition made of clear plastic or wire. The test session began with a 10-min habituation period. A target mouse was placed on one side of the chamber. The subject mouse was placed on the other side of the chamber. The subject mouse can see, hear, and smell the target mouse through the holes in the plastic or wire divider, but physical interactions are blocked. Mice underwent the test for 10 min, after which a new target mouse was introduced for another 10-min test. Mice activities were detected by a camera positioned above the chamber. The time test mice spent within 2 cm of the wire cup was analyzed using ANY-maze software. We calculated the preference index with the ratio of time the test mouse spends with stranger 1 versus stranger 2.

Kinome assay

The animals were anesthetized with isoflurane and immediately decapitated, the brain was harvested and sliced coronally by a mouse brain slicer (Zivic Inc.) between +1.0 and +2.0 mm anterior to bregma, and mPFC tissue was isolated bilaterally using a 1.0-mm Miltex Biopsy Punch (TED PELLA Inc.). Tissues collected from three mice of the sample genotype were pooled and lysed on ice for 30 min using M-PER lysis buffer (Thermo Fisher Scientific, no. 78503) supplemented with Halt Protease and Phosphatase Inhibitor Cocktail (Thermo Fisher Scientific, no. 78440), and protein concentration was quantified by the Pierce BCA Protein Assay Kit (Thermo Fisher Scientific, no. 23227). Samples were diluted to 1 μg/μl and stored at −80°C in aliquots before assayed for kinase activities.

Upstream kinases in *Asic2*$^{-/-}$ or WT mPFC samples were assessed by the PamStation12 system using an STK PamChip (*92*). Each well on the PamChip contains an array of 144 reporter peptides (141 peptide sequences with putative phosphorylation sites specific for STKs and 3 peptides for internal controls). According to the manufacturer's instructions, a mixture of 2 μg of protein from the tissue sample, adenosine triphosphate (ATP), and fluorescein isothiocyanate–labeled anti–phospho-serine/threonine antibodies was loaded on the chip following a 2% bovine serum albumin blocking, and the degrees of phosphorylation on the immobilized peptide substrates were monitored in real-time using Evolve kinetic image capture software. For each peptide, the fluorescence intensities representing peptide phosphorylation were plotted against five time points (10, 20, 50, 100, and 200 ms), and the linear regression analysis was performed to assess the slope and linearity of the signal–exposure time relationship. Peptides that were undetectable or nonlinear ($R^2 < 0.90$) were excluded from subsequent analysis. The linear regression slope of each peptide was multiplied by 100, log2 transformed, and plotted on a heatmap and phosphorylation plot to visualize differences in the global phosphorylation level between *Asic2*$^{-/-}$ and WT samples. The slope ratio of a particular peptide in the *Asic2*$^{-/-}$ sample and in the WT counterpart was calculated to obtain an LFC, and a waterfall plot was generated for a graphical representation of the change in phosphorylation across reporter substrates. On the basis of a list of reporter peptides with LFC greater than 0.2, 0.3, or 0.4, multiple tools including GPS 3.0 (*93*), Kinexus PhosphoNET (Kinexus Bioinformatics), PhosphoELM (http://phospho.elm.eu.org/), and PhosphoSitePlus (*94*) were used to determine potential upstream kinases responsible for the phosphorylation on these substrates, and the frequency of each kinase predicted (observed hits) was obtained, followed by a random sampling analysis conducted using the Kinome Random Sampling Analyzer (KRSA) R software package (*95*). Briefly, a dataset of 2000 data points was generated, and each data point included randomly selected reporter peptides from the kinome array. The number of randomly selected peptides matched the number of peptides with an LFC greater than 0.2, 0.3, or 0.4. The kinases predicted to target these randomly selected peptides were identified, and the frequency of each kinase for all 2000 data points in the dataset was calculated to generate an expected distribution for that kinase. Kinases with observed hits greater than 2 SDs from the mean of their expected

distributions were identified. We used the Kinograte R package, which implements an optimized version of the well-established Prize-Collecting Steiner Forest algorithm, to generate a protein-protein interaction network consisting of kinase "hits" and interpolated "hidden" nodes (*64*). We assigned node prizes by *Z* score percentile rank and edge costs by inverse STRING-DB3 interaction confidence. All data were based on two independent sample sets, in which three *Asic2*$^{-/-}$ mice and three WT mice were used in each set, run in duplicate for kinome analysis. For kinase activity profiling, all instruments, software, and reagents, if not specifically mentioned, were purchased from PamGene ('s-Hertogenbosch, The Netherlands).

Stereotaxic surgery, virus injection, and chemical infusion

For the virus injection procedure, mice were anesthetized with isoflurane through an anesthetic vaporizer, and secured to the stereotaxic instrument (KOPF Model 940 small animal stereotaxic instrument). The AAV_2-CMV-mASIC2-IRES-eGFP was produced based on the *Asic2* mRNA information in Library NIH_MGC_378. The AAV_2-hsyn-Cre-GFP, AAV_2-hsyn-GFP, AAV_2-CaMKIIα-Cre-GFP, and AAV_2-CaMKIIα-GFP were purchased from the University of North Carolina Vector Core. The AAV_2-VGAT1-CRE-EGFP-WPRE-hGH polyA (Biohippo Inc., PT-2328) and AAV_2-VGAT1-EGFP-WPREhGH polyA (Biohippo Inc., no. PT-3176) were purchased from Biohippo Inc. AAVs (0.5 to 1 μl of 10^{13} viral genomes/ml) were injected into the mPFC bilaterally (relative to bregma: +1.9 mm anterioposterior; ±0.3 mm mediolateral; −2.0 mm dorsoventral) using a 10-μl Hamilton microsyringe (Model 1701N) and a WPI microsyringe pump as described previously (*62*). After surgery, mice were housed for 2 weeks before undergoing behavioral, molecular, and electrophysiological tests. The injection sites were identified and the efficiency of the AAVs was evaluated postmortem by sectioning the brain (10 μm coronal), staining the ASIC2, and performing the immunofluorescence staining. In experiments requiring virus injection, data from all mice with "missed" injection sites were excluded from the statistical analysis in the figures.

Brain slice preparation and patch-clamp recording of mPFC neurons

Mice were euthanized with overdosed isoflurane and whole brains were dissected into preoxygenated (5% CO_2 and 95% O_2) ice-cold high-sucrose dissection solution containing 205 mM sucrose, 5 mM KCl, 1.25 mM NaH_2PO_4, 5 mM $MgSO_4$, 26 mM $NaHCO_3$, 1 mM $CaCl_2$, and 25 mM glucose (*29*). A vibratome sliced brains coronally into 300-μm sections that were maintained in normal ACSF containing 115 mM NaCl, 2.5 mM KCl, 2 mM $CaCl_2$, 1 mM $MgCl_2$, 1.25 mM NaH_2PO_4, 11 mM glucose, and 25 mM $NaHCO_3$ bubbled with 95% O_2/5% CO_2, pH 7.35, at 20° to 22°C. Slices were incubated in the ACSF for at least 1 hour before recording. For experiments, individual slices were transferred to a submersion-recording chamber and were continuously perfused with the 5% CO_2/95% O_2 solution (~3.0 ml/min) at room temperature (20° to 22°C).

Pyramidal neurons in the PL subregion of mPFC were studied using whole-cell patch-clamp recordings. The pipette solution contains 135 mM $CsSO_3CH_3$, 5 mM NaCl, 10 mM Hepes, 4 mM MgATP, 0.3 mM Na_3GTP, and 0.5 mM K-EGTA (osmolality = 290, adjusted to pH 7.25 with CsOH). The pipette resistance (measured in the bath solution) was 3 to 5 megohms. High-resistance (>1 gigohms) seals were formed in voltage-clamp mode. Picrotoxin (PTX, 100 μM) was added to the ACSF throughout the recordings to yield excitatory responses except in the mIPSC recording. Constant current pulses (20 to 80 μA, 100 μs, 0.1 Hz) were applied through extracellular bipolar electrodes placed at layer 3 to induce EPSCs in layer 5 in the PL subregion of the mPFC. For injections of acidic ACSF (pH 5.0) to a single neuron in the slice, the acidic ACSF was buffered with 5 mM Hepes and 5 mM MES (115 mM NaCl, 2.5 mM KCl, 2 mM $CaCl_2$, 1 mM $MgCl_2$, 1.25 mM NaH_2PO_4, 11 mM glucose, 5 mM Hepes, and 5 mM MES, pH 5.0, osmolality = 290). Five to ten seconds of acid puff was delivered by a patch-clamp pipette and a microinjector system (Tritech Research Inc). Then, we conducted one patch-clamp recording per neuron in response to one pH application. The decay times (τ) of ASIC currents were best fitted with a single exponential using Clampfit 10.1. In mEPSC experiments, mEPSCs were collected at −80 mV holding potential in the presence of 1 μM tetrodotoxin (TTX) and 100 μM PTX to block Na^+ channels and $GABA_A$ receptors, respectively. In mIPSC experiments, mIPSCs were collected at +60 mV holding potential in the presence of cocktails of 1 μM TTX, 100 μM CNQX, and 100 μM D-APV. In AMPAR current rectification experiments, we applied 100 μM D-APV to block NMDAR-conducted EPSCs. To quantify CP-AMPAR rectification, we supplemented the internal solutions with 100 μM spermidine (Sigma-Aldrich, no. S2626) to offset the dialysis of endogenous polyamines by the patch pipette. The peak amplitude of ESPCs was measured to determine current rectification. The amplitude was measured ranging from −80 to +60 mV in 20-mV steps. The peak amplitude of EPSCs at −80 and +60 mV was measured for the rectification index. To identify the NASPM-sensitive EPSCs, neurons were held at −80 mV in the presence of 100 μM D-APV. NASPM (100 μM) was applied to the slices during recording. In EPSC ratio experiments, neurons were measured at −80 mV to record AMPAR-EPSCs and were measured at +60 mV to record NMDAR-EPSCs. To determine the AMPAR-to-NMDAR ratio, we measured the peak amplitude of ESPCs at −80 mV as AMPAR currents, and the peak amplitude of EPSCs at +60 mV at 70 ms as NMDAR currents after onset.

For resting membrane potential, action potential, and LTP experiments, the neurons were held in current-clamp mode with a pipette solution containing 135 mM KSO_3CH_3, 5 mM NaCl, 10 mM Hepes, 4 mM MgATP, 0.3 mM Na_3GTP, and 0.5 mM K-EGTA (osmolality = 290, adjusted to pH 7.25 with KOH). For the resting membrane potential experiment, the neurons were held in current-clamp mode without current injection. For the action potential experiment, action potentials were elicited by applying a depolarizing stimulus (150 ms) once every 10 s from −400 to +500 pA with a step increase of 100 pA. The spike numbers of action potentials were analyzed. For whole-cell LTP recordings, EPSPs were recorded in current-clamp mode every 10 s as a baseline for 10 min followed by applying an HFS (100 Hz, 1 s) to induce LTP and continuously recorded the EPSCs for at least 1 hour. Data were acquired at 10 kHz using Multiclamp 700B and pClamp 10.1. The mEPSCs events (>5 pA) were analyzed in Clampfit 10.1.

Immunohistochemistry

Following the behavioral procedures indicated in the text and figures, the mice were euthanized with overdosed isoflurane and were subjected to transcardial perfusion with 4% paraformaldehyde (PFA) (Thermo Fisher Scientific, no. AA433689M) to fix whole

brains, followed by continued fixation in 4% PFA at 4°C for 24 hours (*56*). Following perfusion, we used a vibratome (Leica, VT-1000S) to dissect 50-μm PFC coronal slices, which were collected in ice-cold phosphate-buffered saline (PBS). To complete immunofluorescence staining, slices were placed in Superblock solution (Thermo Fisher Scientific, no. 37515) plus 0.2% Triton X-100 for 1 hour before being incubated with primary antibodies at 4°C for 24 hours and rinsed twice in PBS. The slices were then incubated with secondary antibodies for 1 hour at room temperature before being mounted (*29*). Primary antibodies used in this study are anti-ASIC1a antibody (Alomone Labs, no. ASC-014), anti-ASIC2 antibody (Alomone Labs, no. ASC-012), GluA1 polyclonal antibody (Thermo Fisher Scientific, no. PA5-99527), NMDAR2B polyclonal antibody (Innovative Research, no. 71-8600), PKA alpha antibody (Thermo Fisher Scientific, no. MA5-37857), and β-actin antibody (Cell Signaling Technology, no. 4967). Secondary antibodies used in this study are donkey anti-rabbit immunoglobulin G (IgG) (H + L) secondary antibody (Thermo Fisher Scientific, no. A32814 and no. A32754) and donkey anti-mouse IgG (H + L) secondary antibody (Thermo Fisher Scientific, no. A32766 and no. A32744). Slices were mounted using VectaShield H-1500 mounting medium (Vector Laboratories, no. H-1500-10), and images were captured using regular fluorescence and confocal microscopy.

Dendrites and spine morphologic analyses

The mice were euthanized with overdosed isoflurane and were subjected to transcardial perfusion with 1.5% PFA to fix whole brains, followed by continued fixation in 1.5% PFA at 4°C for 6 to 8 hours. We then used a Leica VT1000S vibratome to dissect 248-μm coronal brain slices containing PFC, which were collected in ice-cold PBS. To visualize dendritic spines, the pyramidal neurons in layer 5 in the PL region of the mPFC were filled with Alexa Fluor 568 (Thermo Fisher Scientific, no. A10441) using single-cell microinjections through a whole-cell patch-clamp pipette plus 1 to 10 nA of negative current until dendrites and spines were filled. The brain slice was then mounted on a slide by VectaShield H-1500 mounting medium and covered by a coverslip with a pipe wrap tape (248 μm thickness) as a spacer. The slice was then imaged using a Leica TCS SP5 confocal microscope equipped with the Leica Application Suite software. The filled neurons were visualized with a 63× oil-immersion objective for the final verification of their neuronal types. Individual dendritic segments were focused on and scanned at 0.5-μm intervals along the *z* axis to obtain a z stack. For each neuron, three to five dendritic segments 25 μm in length were analyzed. For each group, 6 to 10 neurons per mouse were analyzed. We used ImageJ software to analyze dendritic branching and spines. The index of dendritic branching was determined by Sholl analysis (intersections over radius) (*59*, *60*). The analysis of dendritic spines including the number of spines, spine density, and spine classification, which are critical indicators of synaptic function, were determined by the following four categories: thin, mushroom, stubby, and filopodia. These spines were categorized based on the following parameters: (i) mushroom spines: head-to-neck diameter ratio > 1.1:1 and spine head diameter > 0.35 μm; (ii) thin spines: head-to-neck diameter ratio > 1.1:1 and spine head diameter > 0.35 μm or spine head-to-neck diameter ratios < 1.1:1 and spine length-to-neck diameter > 2.5 μm; and (iii) stubby spines: spine head-to-neck diameter ratios < 1.1:1 and spine length-to-neck diameter ≤ 2.5 μm (*56*, *71*).

Quantitative real-time PCR and cAMP measurement

Cellular RNA from *Asic2*$^{-/-}$ or WT mouse brain tissue was isolated using TRIzol reagent (Thermo Fisher Scientific, no. 15596026) and reversely transcribed to generate cDNA. Briefly, 2 μg of RNA sample was added into diethylpyrocarbonate-treated water containing random primers (1 μg), heated up to 70°C for 5 min, chilled on ice, and then mixed with Moloney murine leukemia virus reverse transcriptase (200 U), dNTPs (10 mM), ribonuclease inhibitor (50 U) and reaction buffer (all from Promega, Madison, WI) followed by a 60-min incubation at 37°C. Amplification of the cDNA sample was carried out in a mixture of a primer pair targeting the gene of interest and SsoFast EvaGreen Supermix (Bio-Rad, no. 1725200) for 40 cycles of a two-step process (30 s at 95°C and 60 s at 62°C) performed on the Bio-Rad CFX real-time PCR detection system. The CT value was obtained and normalized based on β-actin reading. Primer pairs were supplied from Integrated DNA Technologies: *Asic2* (*Accn1*, Mm.PT.56a.6435803), *Bdnf*(Mm.PT.58.8157970), *Pka* (*Prkaca*, Mm.PT.58.13863331), and β-*Actin* (*Actb*, Mm.PT.39a.22214843.g). Some tissue samples were homogenized in tissue protein extraction reagent (Thermo Fisher Scientific, no. 78503) to prepare cell lysates for cAMP quantification using a direct cAMP ELISA kit (Enzo Life Sciences, no. ADI-900-066). Intracellular cAMP was then analyzed according to the manufacturer's instructions.

Statistical analysis

One-way analysis of variance (ANOVA) and Tukey's post hoc multiple comparison tests were used for the statistical comparison of multiple (≥3) groups. An unpaired Student's *t* test was used to compare results between the two groups. $P < 0.05$ was considered statistically significant, and we did not exclude potential outliers from our data except the ones that met our exclusion criteria (refer to the individual Materials and Methods sections for details). The graphing and statistical analysis software GraphPad Prism 8 was used to analyze statistical data, which was presented as means ± SEM. Sample sizes (*n*) are indicated in the figure legends, and data are reported as biological replicates (data from different mice and different brain slices). Each group contained tissues pooled from four to five mice. Because of variable behavior within groups, we used sample sizes of 10 to 16 mice per experimental group as we previously described in earlier experiments (*29*). In behavioral studies, animals were randomly assigned to experimental groups based solely on their cage numbers. We ensured that the randomization is stratified by relevant factors, such as age, sex, and weight, to achieve balanced groups (see the "Animals" section). We typically studied groups with four randomly assigned animals per group, as our recording equipment allowed us to record four separate animal cages simultaneously. The experiments were repeated with another set of four animals until we reached the target number of experimental mice per group. Experimentation groups were repeated in this manner so that each animal had the same controlled environment, the same time of day, and similar handling, habituation, and processes. Most behavioral experiments were replicated at least four times. The key social dominance experiments were replicated >10 times. Western blot, Kinome assay, immunohistochemistry, dendrite analyses, and other molecular experiments were replicated three to four times. Electrophysiology experiments were replicated four to five times. Both the researchers conducting the experiments and those analyzing the data will be blinded to the group assignments. In addition, outcome assessments were reviewed by independent evaluators who were unaware of the treatment groups.

Supplementary Materials

This PDF file includes:

Figs. S1 to S13

REFERENCES AND NOTES

1. A. Baum, J. P. Garofalo, A. M. Yali, Socioeconomic status and chronic stress: Does stress account for SES effects on health? *Ann. N. Y. Acad. Sci.* **896**, 131–144 (1999).
2. M. Davari, M. R. Maracy, E. Khorasani, Socioeconomic status, cardiac risk factors, and cardiovascular disease: A novel approach to determination of this association. *ARYA Atheroscler* **15**, 260–266 (2019).
3. I. Kawachi, S. V. Subramanian, N. Almeida-Filho, A glossary for health inequalities. *J. Epidemiol. Community Health* **56**, 647–652 (2002).
4. R. Ennals, Michael Marmot (2004) Status Syndrome: How your social standing directly affects your health and life expectancy. *AI Soc.* **21**, 231–233 (2006).
5. F. H. Bronson, The reproductive ecology of the house mouse. *Q. Rev. Biol.* **54**, 265–299 (1979).
6. C. M. Williamson, W. Lee, A. R. DeCasien, A. Lanham, R. D. Romeo, J. P. Curley, Social hierarchy position in female mice is associated with plasma corticosterone levels and hypothalamic gene expression. *Sci. Rep.* **9**, 7324 (2019).
7. F. Wang, J. Zhu, H. Zhu, Q. Zhang, Z. Lin, H. Hu, Bidirectional control of social hierarchy by synaptic efficacy in medial prefrontal cortex. *Science* **334**, 693–697 (2011).
8. T. Zhou, H. Zhu, Z. Fan, F. Wang, Y. Chen, H. Liang, Z. Yang, L. Zhang, L. Lin, Y. Zhan, Z. Wang, H. Hu, History of winning remodels thalamo-PFC circuit to reinforce social dominance. *Science* **357**, 162–168 (2017).
9. A. C. Nelson, V. Kapoor, E. Vaughn, J. A. Gnanasegaram, N. D. Rubinstein, V. N. Murthy, C. Dulac, Molecular and circuit architecture of social hierarchy. bioRxiv 838664 [Preprint] (2019). https://biorxiv.org/content/10.1101/838664v1.
10. N. Padilla-Coreano, K. Batra, M. Patarino, Z. Chen, R. R. Rock, R. Zhang, S. B. Hausmann, J. C. Weddington, R. Patel, Y. E. Zhang, H. S. Fang, S. Mishra, D. O. LeDuke, J. Revanna, H. Li, M. Borio, R. Pamintuan, A. Bal, L. R. Keyes, A. Libster, R. Wichmann, F. Mills, F. H. Taschbach, G. A. Matthews, J. P. Curley, I. R. Fiete, C. Lu, K. M. Tye, Cortical ensembles orchestrate social competition through hypothalamic outputs. *Nature* **603**, 667–671 (2022).
11. L. Kingsbury, S. Huang, J. Wang, K. Gu, P. Golshani, Y. E. Wu, W. Hong, Correlated neural activity and encoding of behavior across brains of socially interacting animals. *Cell* **178**, 429–446.e16 (2019).
12. J. Du, L. R. Reznikov, M. P. Price, X. M. Zha, Y. Lu, T. O. Moninger, J. A. Wemmie, M. J. Welsh, Protons are a neurotransmitter that regulates synaptic plasticity in the lateral amygdala. *Proc. Natl. Acad. Sci. U.S.A.* **111**, 8961–8966 (2014).
13. H. Kawasaki, S. Eguchi, S. Miyashita, S. Chan, K. Hirai, N. Hobara, A. Yokomizo, H. Fujiwara, Y. Zamami, T. Koyama, X. Jin, Y. Kitamura, Proton acts as a neurotransmitter for nicotine-induced adrenergic and calcitonin gene-related peptide-containing nerve-mediated vasodilation in the rat mesenteric artery. *J. Pharmacol. Exp. Ther.* **330**, 745–755 (2009).
14. S. M. Highstein, G. R. Holstein, M. A. Mann, R. D. Rabbitt, Evidence that protons act as neurotransmitters at vestibular hair cell-calyx afferent synapses. *Proc. Natl. Acad. Sci. U.S.A.* **111**, 5421–5426 (2014).
15. M. Chesler, Regulation and modulation of pH in the brain. *Physiol. Rev.* **83**, 1183–1221 (2003).
16. R. Waldmann, G. Champigny, F. Bassilana, C. Heurteaux, M. Lazdunski, A proton-gated cation channel involved in acid-sensing. *Nature* **386**, 173–177 (1997).
17. R. Waldmann, M. Lazdunski, H^+-gated cation channels: Neuronal acid sensors in the NaC/DEG family of ion channels. *Curr. Opin. Neurobiol.* **8**, 418–424 (1998).
18. J. A. Wemmie, R. J. Taugher, C. J. Kreple, Acid-sensing ion channels in pain and disease. *Nat. Rev. Neurosci.* **14**, 461–471 (2013).
19. S. Grunder, M. Pusch, Biophysical properties of acid-sensing ion channels (ASICs). *Neuropharmacology* **94**, 9–18 (2015).
20. D. M. MacLean, V. Jayaraman, Acid-sensing ion channels are tuned to follow high-frequency stimuli. *J. Physiol.* **594**, 2629–2645 (2016).
21. T. W. Sherwood, K. G. Lee, M. G. Gormley, C. C. Askwith, Heteromeric acid-sensing ion channels (ASICs) composed of ASIC2b and ASIC1a display novel channel properties and contribute to acidosis-induced neuronal death. *J. Neurosci.* **31**, 9723–9734 (2011).
22. J. A. Wemmie, J. Chen, C. C. Askwith, A. M. Hruska-Hageman, M. P. Price, B. C. Nolan, P. G. Yoder, E. Lamani, T. Hoshi, J. H. Freeman Jr., M. J. Welsh, The acid-activated ion channel ASIC contributes to synaptic plasticity, learning, and memory. *Neuron* **34**, 463–477 (2002).
23. W. Zhou, S. Ye, R. Luo, L.-M. Wu, W. Wang, Inhibition of acid-sensing ion channels reduces the hypothalamus–pituitary–adrenal axis activity and ameliorates depression-like behavior in rats. *RSC Adv.* **9**, 8707–8713 (2019).
24. K. A. Sluka, O. C. Winter, J. A. Wemmie, Acid-sensing ion channels: A new target for pain and CNS diseases. *Curr. Opin. Drug Discov. Devel.* **12**, 693–704 (2009).
25. Y. Aissouni, A. El Guerrab, A. M. Hamieh, J. Ferrier, M. Chalus, D. Lemaire, S. Gregoire, M. Etienne, A. Eschalier, D. Ardid, E. Lingueglia, F. Marchand, Acid-sensing ion channel 1a in the amygdala is involved in pain and anxiety-related behaviours associated with arthritis. *Sci. Rep.* **7**, 43617 (2017).
26. W.-L. Wu, Y.-W. Lin, M.-Y. Min, C.-C. Chen, Mice lacking *Asic3* show reduced anxiety-like behavior on the elevated plus maze and reduced aggression. *Genes Brain Behav.* **9**, 603–614 (2010).
27. A. E. Ziemann, J. E. Allen, N. S. Dahdaleh, I. I. Drebot, M. W. Coryell, A. M. Wunsch, C. M. Lynch, F. M. Faraci, M. J. Howard III, M. J. Welsh, J. A. Wemmie, The amygdala is a chemosensor that detects carbon dioxide and acidosis to elicit fear behavior. *Cell* **139**, 1012–1021 (2009).
28. M. W. Coryell, A. M. Wunsch, J. M. Haenfler, J. E. Allen, J. L. McBride, B. L. Davidson, J. A. Wemmie, Restoring acid-sensing ion channel-1a in the amygdala of knock-out mice rescues fear memory but not unconditioned fear responses. *J. Neurosci.* **28**, 13738–13741 (2008).
29. J. Du, M. P. Price, R. J. Taugher, D. Grigsby, J. J. Ash, A. C. Stark, M. Z. Hossain Saad, K. Singh, J. Mandal, J. A. Wemmie, M. J. Welsh, Transient acidosis while retrieving a fear-related memory enhances its lability. *eLife* **6**, e22564 (2017).
30. Q. Wang, Q. Wang, X. L. Song, Q. Jiang, Y. J. Wu, Y. Li, T. F. Yuan, S. Zhang, N. J. Xu, M. X. Zhu, W. G. Li, T. L. Xu, Fear extinction requires ASIC1a-dependent regulation of hippocampal-prefrontal correlates. *Sci. Adv.* **4**, eaau3075 (2018).
31. A. L. Gutman, C. V. Cosme, M. F. Noterman, W. R. Worth, J. A. Wemmie, R. T. LaLumiere, Overexpression of ASIC1A in the nucleus accumbens of rats potentiates cocaine-seeking behavior. *Addict. Biol.* **25**, e12690 (2020).
32. M. W. Coryell, A. M. Wunsch, J. M. Haenfler, J. E. Allen, M. Schnizler, A. E. Ziemann, M. N. Cook, J. P. Dunning, M. P. Price, J. D. Rainier, Z. Liu, A. R. Light, D. R. Langbehn, J. A. Wemmie, Acid-sensing ion channel-1a in the amygdala, a novel therapeutic target in depression-related behavior. *J. Neurosci.* **29**, 5381–5388 (2009).
33. M. P. Price, H. Gong, M. G. Parsons, J. R. Kundert, L. R. Reznikov, L. Bernardinelli, K. Chaloner, G. F. Buchanan, J. A. Wemmie, G. B. Richerson, M. D. Cassell, M. J. Welsh, Localization and behaviors in null mice suggest that ASIC1 and ASIC2 modulate responses to aversive stimuli. *Genes Brain Behav.* **13**, 179–194 (2014).
34. Z. Fan, H. Zhu, T. Zhou, S. Wang, Y. Wu, H. Hu, Using the tube test to measure social hierarchy in mice. *Nat. Protoc.* **14**, 819–831 (2019).
35. C. Drews, The concept and definition of dominance in animal behaviour. *Behaviour* **125**, 283–313 (1993).
36. C. Roza, J. L. Puel, M. Kress, A. Baron, S. Diochot, M. Lazdunski, R. Waldmann, Knockout of the ASIC2 channel in mice does not impair cutaneous mechanosensation, visceral mechanonociception and hearing. *J. Physiol.* **558**, 659–669 (2004).
37. K. L. Laskowski, M. Wolf, D. Bierbach, The making of winners (and losers): How early dominance interactions determine adult social structure in a clonal fish. *Proc. Biol. Sci.* **283**, 20160183 (2016).
38. Y. Hsu, R. L. Earley, L. L. Wolf, Modulation of aggressive behaviour by fighting experience: Mechanisms and contest outcomes. *Biol. Rev. Camb. Philos. Soc.* **81**, 33–74 (2006).
39. C. F. Zink, Y. Tong, Q. Chen, D. S. Bassett, J. L. Stein, A. Meyer-Lindenberg, Know your place: Neural processing of social hierarchy in humans. *Neuron* **58**, 273–283 (2008).
40. D. M. Amodio, C. D. Frith, Meeting of minds: The medial frontal cortex and social cognition. *Nat. Rev. Neurosci.* **7**, 268–277 (2006).
41. R. R. Holson, Mesial prefrontal cortical lesions and timidity in rats. III. Behavior in a semi-natural environment. *Physiol. Behav.* **37**, 239–247 (1986).
42. R. R. Holson, Mesial prefrontal cortical lesions and timidity in rats. I. Reactivity to aversive stimuli. *Physiol. Behav.* **37**, 221–230 (1986).
43. R. R. Holson, C. Walker, Mesial prefrontal cortical lesions and timidity in rats. II. Reactivity to novel stimuli. *Physiol. Behav.* **37**, 231–238 (1986).
44. D. Wei, V. Talwar, D. Lin, Neural circuits of social behaviors: Innate yet flexible. *Neuron* **109**, 1600–1620 (2021).
45. Z. Guo, L. Yin, V. Diaz, B. Dai, T. Osakada, J. E. Lischinsky, J. Chien, T. Yamaguchi, A. Urtecho, X. Tong, Z. S. Chen, D. Lin, Neural dynamics in the limbic system during male social behaviors. *Neuron* **111**, 3288–3306.e4 (2023).
46. B. Yang, T. Karigo, D. J. Anderson, Transformations of neural representations in a social behaviour network. *Nature* **608**, 741–749 (2022).
47. S. C. Gupta, A. Ghobbeh, R. J. Taugher-Hebl, R. Fan, J. B. Hardie, R. T. LaLumiere, J. A. Wemmie, Carbonic anhydrase 4 disruption decreases synaptic and behavioral adaptations induced by cocaine withdrawal. *Sci. Adv.* **8**, eabq5058 (2022).
48. S. Cull-Candy, L. Kelly, M. Farrant, Regulation of Ca^{2+}–permeable AMPA receptors: Synaptic plasticity and beyond. *Curr. Opin. Neurobiol.* **16**, 288–297 (2006).
49. S. G. Cull-Candy, M. Farrant, Ca^{2+}-permeable AMPA receptors and their auxiliary subunits in synaptic plasticity and disease. *J. Physiol.* **599**, 2655–2671 (2021).
50. P. M. Matthews, A. Pinggera, D. Kampjut, I. H. Greger, Biology of AMPA receptor interacting proteins—From biogenesis to synaptic plasticity. *Neuropharmacology* **197**, 108709 (2021).

51. W. J. Korzan, E. Hoglund, M. J. Watt, G. L. Forster, O. Overli, J. L. Lukkes, C. H. Summers, Memory of opponents is more potent than visual sign stimuli after social hierarchy has been established. *Behav. Brain Res.* **183**, 31–42 (2007).
52. M. I. Cordero, C. Sandi, Stress amplifies memory for social hierarchy. *Front. Neurosci.* **1**, 175–184 (2007).
53. Y.-J. Chou, Y.-K. Ma, Y.-H. Lu, J.-T. King, W.-S. Tasi, S.-B. Yang, T.-H. Kuo, Potential cross-species correlations in social hierarchy and memory between mice and young children. *Commun. Biol.* **5**, 230 (2022).
54. D. S. K. Samways, A. B. Harkins, T. M. Egan, Native and recombinant ASIC1a receptors conduct negligible Ca^{2+} entry. *Cell Calcium* **45**, 319–325 (2009).
55. M.-G. Liu, H.-S. Li, W.-G. Li, Y.-J. Wu, S.-N. Deng, C. Huang, O. Maximyuk, V. Sukach, O. Krishtal, M. X. Zhu, T. L. Xu, Acid-sensing ion channel 1a contributes to hippocampal LTP inducibility through multiple mechanisms. *Sci. Rep.* **6**, 23350 (2016).
56. W. J. Wright, N. M. Graziane, P. A. Neumann, P. J. Hamilton, H. M. Cates, L. Fuerst, A. Spenceley, N. MacKinnon-Booth, K. Iyer, Y. H. Huang, Y. Shaham, O. M. Schluter, E. J. Nestler, Y. Dong, Silent synapses dictate cocaine memory destabilization and reconsolidation. *Nat. Neurosci.* **23**, 32–46 (2020).
57. K. M. Woolfrey, D. P. Srivastava, Control of dendritic spine morphological and functional plasticity by small GTPases. *Neural Plast.* **2016**, 3025948 (2016).
58. G. Yang, F. Pan, W. B. Gan, Stably maintained dendritic spines are associated with lifelong memories. *Nature* **462**, 920–924 (2009).
59. D. A. Sholl, Dendritic organization in the neurons of the visual and motor cortices of the cat. *J. Anat.* **87**, 387–406 (1953).
60. L. Rietveld, D. P. Stuss, D. McPhee, K. R. Delaney, Genotype-specific effects of *Mecp2* loss-of-function on morphology of layer V pyramidal neurons in heterozygous female Rett syndrome model mice. *Front. Cell. Neurosci.* **9**, 145 (2015).
61. K. P. Berry, E. Nedivi, Spine dynamics: Are they all the same? *Neuron* **96**, 43–55 (2017).
62. E. E. Koffman, C. M. Kruse, K. Singh, F. S. Naghavi, M. A. Curtis, J. Egbo, M. Houdi, B. Lin, H. Lu, J. Debiec, J. Du, Acid-sensing ion channel 1a regulates the specificity of reconsolidation of conditioned threat responses. *JCI Insight* **7**, e155341 (2022).
63. S. I. Walaas, P. Greengard, Protein phosphorylation and neuronal function. *Pharmacol. Rev.* **43**, 299–349 (1991).
64. K. Alganem, A.-R. Hamoud, J. F. Creeden, N. D. Henkel, A. S. Imami, A. W. Joyce, V. W. Ryan, J. B. Rethman, R. Shukla, S. M. O'Donovan, J. Meller, R. McCullumsmith, The active kinome: The modern view of how active protein kinase networks fit in biological research. *Curr. Opin. Pharmacol.* **62**, 117–129 (2022).
65. B. Shamsaei, S. Chojnacki, M. Pilarczyk, M. Najafabadi, W. Niu, C. Chen, K. Ross, A. Matlock, J. Muhlich, S. Chutipongtanate, J. Zheng, J. Turner, D. Vidovic, J. Jaffe, M. MacCoss, C. Wu, A. Pillai, A. Ma'ayan, S. Schurer, M. Kouril, M. Medvedovic, J. Meller, piNET: A versatile web platform for downstream analysis and visualization of proteomics data. *Nucleic Acids Res.* **48**, W85–W93 (2020).
66. A. L. Carvalho, C. B. Duarte, A. P. Carvalho, Regulation of AMPA receptors by phosphorylation. *Neurochem. Res.* **25**, 1245–1255 (2000).
67. Y. Pen, N. Borovok, M. Reichenstein, A. Sheinin, I. Michaelevski, Membrane-tethered AKT kinase regulates basal synaptic transmission and early phase LTP expression by modulation of post-synaptic AMPA receptor level. *Hippocampus* **26**, 1149–1167 (2016).
68. H.-Y. Man, Q. Wang, W.-Y. Lu, W. Ju, G. Ahmadian, L. Liu, S. D'Souza, T. P. Wong, C. Taghibiglou, J. Lu, L. E. Becker, L. Pei, F. Liu, M. P. Wymann, J. F. MacDonald, Y. T. Wang, Activation of PI3-kinase is required for AMPA receptor insertion during LTP of mEPSCs in cultured hippocampal neurons. *Neuron* **38**, 611–624 (2003).
69. Y. Ikegaya, M. Le Bon-Jego, R. Yuste, Large-scale imaging of cortical network activity with calcium indicators. *Neurosci. Res.* **52**, 132–138 (2005).
70. Y. Song, Q. X. Meng, K. Wu, R. Hua, Z. J. Song, Y. Song, X. Qin, J. L. Cao, Y. M. Zhang, Disinhibition of PVN-projecting GABAergic neurons in AV region in BNST participates in visceral hypersensitivity in rats. *Psychoneuroendocrinology* **117**, 104690 (2020).
71. C. J. Kreple, Y. Lu, R. J. Taugher, A. L. Schwager-Gutman, J. Du, M. Stump, Y. Wang, A. Ghobbeh, R. Fan, C. V. Cosme, L. P. Sowers, M. J. Welsh, J. J. Radley, R. T. LaLumiere, J. A. Wemmie, Acid-sensing ion channels contribute to synaptic transmission and inhibit cocaine-evoked plasticity. *Nat. Neurosci.* **17**, 1083–1091 (2014).
72. K. Kaila, B. R. Ransom, *pH and Brain Function* (Wiley-Liss, ed. 1, 1998).
73. B. C. Trainor, K. K. Crean, W. H. D. Fry, C. Sweeney, Activation of extracellular signal-regulated kinases in social behavior circuits during resident-intruder aggression tests. *Neuroscience* **165**, 325–336 (2010).
74. M. J. Berridge, The interaction of cyclic nucleotides and calcium in the control of cellular activity. *Adv. Cyclic Nucleotide Res.* **6**, 1–98 (1975).
75. A. E. Bugrim, Regulation of Ca^{2+} release by cAMP-dependent protein kinase. A mechanism for agonist-specific calcium signaling? *Cell Calcium* **25**, 219–226 (1999).
76. J. I. E. Bruce, S. V. Straub, D. I. Yule, Crosstalk between cAMP and Ca^{2+} signaling in non-excitable cells. *Cell Calcium* **34**, 431–444 (2003).
77. L. N. Borodinsky, N. C. Spitzer, Second messenger pas de deux: The coordinated dance between calcium and cAMP. *Sci. STKE* **2006**, pe22 (2006).
78. T. Abel, P. V. Nguyen, M. Barad, T. A. Deuel, E. R. Kandel, R. Bourtchouladze, Genetic demonstration of a role for PKA in the late phase of LTP and in hippocampus-based long-term memory. *Cell* **88**, 615–626 (1997).
79. C. Isiegas, A. Park, E. R. Kandel, T. Abel, K. M. Lattal, Transgenic inhibition of neuronal protein kinase A activity facilitates fear extinction. *J. Neurosci.* **26**, 12700–12707 (2006).
80. R. Bernabeu, L. Bevilaqua, P. Ardenghi, E. Bromberg, P. Schmitz, M. Bianchin, I. Izquierdo, J. H. Medina, Involvement of hippocampal cAMP/cAMP-dependent protein kinase signaling pathways in a late memory consolidation phase of aversively motivated learning in rats. *Proc. Natl. Acad. Sci. U.S.A.* **94**, 7041–7046 (1997).
81. M. Barad, R. Bourtchouladze, D. G. Winder, H. Golan, E. Kandel, Rolipram, a type IV-specific phosphodiesterase inhibitor, facilitates the establishment of long-lasting long-term potentiation and improves memory. *Proc. Natl. Acad. Sci. U.S.A.* **95**, 15020–15025 (1998).
82. J. Ahi, J. Radulovic, J. Spiess, The role of hippocampal signaling cascades in consolidation of fear memory. *Behav. Brain Res.* **149**, 17–31 (2004).
83. J. Quevedo, M. R. M. Vianna, M. R. Martins, T. Barichello, J. H. Medina, R. Roesler, I. Izquierdo, Protein synthesis, PKA, and MAP kinase are differentially involved in short- and long-term memory in rats. *Behav. Brain Res.* **154**, 339–343 (2004).
84. I. M. Amaral, C. Lemos, I. Cera, G. Dechant, A. Hofer, R. El Rawas, Involvement of cAMP-dependent protein kinase in the nucleus accumbens in cocaine versus social interaction reward. *Int. J. Mol. Sci.* **22**, 345 (2020).
85. M. Storozhuk, A. Cherninskyi, O. Maximyuk, D. Isaev, O. Krishtal, Acid-sensing ion channels: Focus on physiological and some pathological roles in the brain. *Curr. Neuropharmacol.* **19**, 1570–1589 (2021).
86. Y. Egashira, M. Takase, S. Watanabe, J. Ishida, A. Fukamizu, R. Kaneko, Y. Yanagawa, S. Takamori, Unique pH dynamics in GABAergic synaptic vesicles illuminates the mechanism and kinetics of GABA loading. *Proc. Natl. Acad. Sci. U.S.A.* **113**, 10702–10707 (2016).
87. P.-H. Chiang, T.-C. Chien, C.-C. Chen, Y. Yanagawa, C.-C. Lien, ASIC-dependent LTP at multiple glutamatergic synapses in amygdala network is required for fear memory. *Sci. Rep.* **5**, 10143 (2015).
88. M. Storozhuk, E. Kondratskaya, L. Nikolaenko, O. Krishtal, A modulatory role of ASICs on GABAergic synapses in rat hippocampal cell cultures. *Mol. Brain* **9**, 90 (2016).
89. E. Ferreira-Fernandes, J. Peca, The neural circuit architecture of social hierarchy in rodents and primates. *Front. Cell. Neurosci.* **16**, 874310 (2022).
90. H. Leblanc, S. Ramirez, Linking social cognition to learning and memory. *J. Neurosci.* **40**, 8782–8798 (2020).
91. B. Rein, K. Ma, Z. Yan, A standardized social preference protocol for measuring social deficits in mouse models of autism. *Nat. Protoc.* **15**, 3464–3477 (2020).
92. J. F. Creeden, Z. A. Kipp, M. Xu, R. M. Flight, H. N. B. Moseley, G. J. Martinez, W.-H. Lee, K. Alganem, A. S. Imami, M. R. McMullen, S. Roychowdhury, A. M. Nawabi, J. A. Hipp, S. Softic, S. A. Weinman, R. McCullumsmith, L. E. Nagy, T. D. Hinds Jr., Hepatic kinome atlas: An in-depth identification of kinase pathways in liver fibrosis of humans and rodents. *Hepatology* **76**, 1376–1388 (2022).
93. Y. Xue, J. Ren, X. Gao, C. Jin, L. Wen, X. Yao, GPS 2.0, a tool to predict kinase-specific phosphorylation sites in hierarchy. *Mol. Cell. Proteomics* **7**, 1598–1608 (2008).
94. P. V. Hornbeck, J. M. Kornhauser, S. Tkachev, B. Zhang, E. Skrzypek, B. Murray, V. Latham, M. Sullivan, PhosphoSitePlus: A comprehensive resource for investigating the structure and function of experimentally determined post-translational modifications in man and mouse. *Nucleic Acids Res.* **40**, D261–D270 (2012).
95. E. A. K. DePasquale, K. Alganem, E. Bentea, N. Nawreen, J. L. McGuire, T. Tomar, F. Naji, R. Hilhorst, J. Meller, R. E. McCullumsmith, KRSA: An R package and R Shiny web application for an end-to-end upstream kinase analysis of kinome array data. *PLOS ONE* **16**, e0260440 (2021).

Acknowledgments: We thank M. Welsh and J. Wemmie at the University of Iowa for providing the *Asic2*$^{-/-}$ and *Asic1a*$^{-/-}$ mice. We thank E. Tolley and R. Zhu in BERD Clinic at UTHSC for statistical support. **Funding:** J.D. is supported by the NIMH (R01MH113986), the Cystic Fibrosis Foundation (002544I221), and the University of Tennessee Health Science Center start-up fund. R.E.M. is supported by the NIMH (R01MH107487). H.L. is supported by the NINDS (R01NS118197). W.G.R. is supported by the NIH NIGMS T32-G-RISE grant 1T32GM144873-01. **Author contributions:** Conceptualization: J.D., B.L., and H.L. Methodology: J.D., B.L., Z.J., Q.G., A.S.I., K.S., H.L., and R.E.M. Investigation: J.D., B.L., Z.J., G.P., Q.G., F.N., W.G.R., K.S., O.A.M, A.S.I., S.K., and R.E.M. Validation: J.D., B.L., Z.J., G.P., Q.G., A.S.I., K.S., O.A.M, S.K., H.L., and R.E.M. Visualization: J.D., B.L., Z.J., G.P., A.S.I., W.G.R., H.L., and R.E.M. Formal analysis: J.D., B.L., Z.J., G.P., Q.G., A.S.I., S.K., K.S., F.N., O.A.M, H.L., W.G.R., and R.E.M. Software: A.S.I. and W.G.R. Project administration: J.D. Supervision: J.D., H.L., and R.E.M. Resources: J.D. and R.E.M. Data curation: J.D., B.L., Z.J., Q.G., A.S.I., K.S., S.K., W.G.R., and R.E.M. Funding acquisition: J.D., H.L., and R.E.M. Writing—original draft: J.D. and B.L. Writing—review and editing: J.D., B.L., Z.J., G.P., Q.G., O.A.M, H.L., W.G.R., and R.E.M. **Competing interests:** The authors declare that they have no competing interests. **Data and materials**

availability: All data needed to evaluate the conclusions in the paper are present in the paper and/or the Supplementary Materials. The *Asic2*$^{-/-}$ and *Asic1a*$^{-/-}$ mice can be provided by M. Welsh and J. Wemmie pending scientific review and a completed material transfer agreement. Requests for these mice should be submitted to M. Welsh and J. Wemmie. The *Asic2*$^{f/f}$ mice can be provided by J. Du pending scientific review and a completed material transfer agreement. Requests for the *Asic2*$^{f/f}$ mice should be submitted to J. Du. The raw reads for the proteomic data generated in this study have been deposited in Zenodo under this DOI: doi/10.5281/zenodo.10119850 and https://zenodo.org/doi/10.5281/zenodo.10119850.

Submitted 27 December 2023
Accepted 23 September 2024
Published 25 October 2024
10.1126/sciadv.adn7573